Cosserat-phase-field modeling of grain nucleation in plastically deformed single crystals

Flavien Ghiglione, Anna Ask, Kais Ammar, Benoît Appolaire, Samuel Forest

Cosserat-phase-field modeling of grain nucleation in plastically deformed single crystals

Flavien GHIGLIONE[a], Anna ASK[b], Kais AMMAR[a], Benoît APPOLAIRE[c,d], Samuel FOREST[a]

[a]*Mines Paris, PSL University, Centre des matériaux, CNRS UMR 7633, BP 87, 91003 Evry, France*
[b]*Département Matériaux et Structures, Onera, BP 72, 92322 Châtillon CEDEX, France*
[c]*Université de Lorraine, CNRS, IJL, 2 allée André Guinier, 54000 Nancy, France*
[d]*Labex Damas, Université de Lorraine, Nancy, France*

Abstract

Thermomechanical processing of crystalline materials induces microstructural evolution such as grain nucleation and growth. In the numerical simulation of these processes, grain nucleation is generally treated as an additional *ad hoc* step in which circular or spherical grains are added in regions where a critical dislocation density, stress or strain are reached. In this paper, systematic finite element simulations are performed showing that the Kobayashi-Warren-Carter (KWC) phase field model and its coupling with Cosserat crystal plasticity predict spontaneous nucleation of new grains in single crystals in the presence of lattice orientation/rotation gradients. The numerical analysis of the stability of gradients of lattice rotation and dislocation-based stored energy indicates that a gradient of stored energy alone is not sufficient to trigger grain formation. As an application, the KWC-Cosserat model is used to simulate the torsion and annealing of a copper single crystal bar with a circular cross section. This mechanical loading produces a large, fairly uniform axial rotation gradient which induces nucleation in the form of a stack of cylindrical grains. Plastic strain gradients in cross-sections predicted by the 3D finite element simulation, are not strong enough to compete with the longitudinal nucleation process, as confirmed by experimental observations from the literature.

Keywords: Cosserat crystal plasticity, KWC phase field model, grain nucleation, recrystallization

1. Introduction

Thermomechanical processing of crystalline materials induces significant microstructural changes such as recrystallization, a restoration process in which new dislocation-free grains are nucleated and grow upon further annealing (Rollett et al., 2017). Although the growth of recrystallized grains is fairly well understood and simulated, uncertainties remain to be resolved in order to properly model the nucleation stage of recrystallization. The main mechanisms generally accepted by the scientific community include strain induced boundary migration (SIBM) and subgrain coarsening, while a third, referred to as subgrain coalescence, is still under debate (Doherty et al., 1997; Rios et al., 2005; Raabe, 2014; Rollett et al., 2017; Ferdinand Knipschildt, 2022). Strain induced boundary migration (Beck and Sperry, 1950) consists of a pre-existing high angle grain boundary growing into a grain with a higher dislocation content. Subgrain coarsening (Beck, 1949; Cahn, 1950) describes the thermally assisted growth of a subgrain at the expense of its surrounding neighbors. Subgrain coalescence is the rotation of two adjacent subgrains to align their lattices and form

Email addresses: flavien.ghiglione@minesparis.psl.eu (Flavien GHIGLIONE), anna.ask@onera.fr (Anna ASK), kais.ammar@minesparis.psl.eu (Kais AMMAR), benoit.appolaire@univ-lorraine.fr (Benoît APPOLAIRE), samuel.forest@minesparis.psl.eu (Samuel FOREST)

a larger subgrain with increased orientation difference with respect to the surrounding matrix. Recrystallization occurs preferentially at sites of large orientation gradients, such as grain boundaries (GB) and triple junctions, where lattice misorientation accumulates (Rollett et al., 2017). Large orientation gradients can also result from heterogeneous deformation. For example, transition bands are bands of high lattice strain that separate regions of different orientations in a grain that has split during deformation. Shear bands are another example of preferential nucleation sites due to heterogeneous deformation. They consist of thin regions of highly strained material associated with large stored energy and orientation gradients across the band.

A wide variety of techniques have been developed to model recrystallization in full-field simulations, including Monte-Carlo Potts (Anderson et al., 1984; Gao and Thompson, 1996; Raabe, 2000; Liu and Lusk, 2002; Mason et al., 2015), cellular automata (Hesselbarth and Göbel, 1991; Liu et al., 1996; Raabe, 1998; Sitko et al., 2020), level sets (Bernacki et al., 2008; Scholtes et al., 2016; Sarrazola et al., 2020a,b) and phase field models. In the latter approach, interfaces are represented as continuous and diffuse fields varying across a narrow region. These models are thermodynamically consistent and sharp interface properties can be recovered as a limit case (Elder et al., 2001). Within this paradigm, two main strategies have emerged: one in which there is one phase field variable per grain (Chen and Yang, 1994; Steinbach and Pezzolla, 1999), and one in which there are only two independent phase field variables for the whole polycrystalline microstructure (Kobayashi et al., 2000; Warren et al., 2003), referred to as the Kobayashi-Warren-Carter (KWC) model. Initially, both approaches to phase field modeling of microstructure evolution were developed to capture grain growth due to grain boundary energy and curvature. As such, they do not incorporate mechanical effects and therefore cannot account for microstructural changes induced by viscoplastic deformation. However, by virtue of their thermodynamic formulation, phase field models can be easily extended to multiphysics. Indeed, other physical contributions such as elastic strain or stored energy can be taken into account by adding them to the free energy functional (Steinbach and Apel, 2006). Classically, phase field (and level set) models are coupled with crystal plasticity in staggered schemes. The nucleation step is handled by placing a circular/spherical nucleus at grain boundaries based on a critical strain, stress or dislocation density criterion. This *ad hoc* step can be deterministic or probabilistic as in Li et al. (2020). Examples of such coupling in the multiple phase field approach to simulate static and dynamic recrystallization can be found in (Steinbach and Apel, 2006; Takaki et al., 2008a; Takaki and Tomita, 2010) with extension to 3D by Chen et al. (2015); as for the KWC model, examples can be found in (Takaki et al., 2008b), (Abrivard et al., 2012a,b) and more recently in (Luan et al., 2020). In addition to these staggered schemes, monolithic algorithms have also been established to solve the coupled equations. In this context, two approaches based on generalized continua have been proposed in (Admal et al., 2018; He and Admal, 2021a) and (Ask et al., 2018a,b, 2019, 2020). They provide a unified and thermodynamically consistent way of modeling microstructural changes accounting for concomitant deformation and grain boundary motion. The common feature of these models is the identification of the lattice orientation gradient in the KWC free energy with a generalized strain measure: the geometrically necessary dislocation density tensor (Nye, 1953) in (Admal et al., 2018) and the Cosserat lattice curvature tensor in (Ask et al., 2018b).

The Cosserat continuum, also called micropolar in (Kafadar and Eringen, 1971), enriches the classical description by attaching to each material point a triad of orthogonal directors that can undergo rigid body rotations. This theory incorporates information about the underlying microstructure and introduces the torsion-curvature tensor as a deformation measure through the first gradient of Cosserat microrotation. As explained by Nye (1953), the state of dislocations represented by the dislocation density tensor is closely related to crystal lattice curvature, leading to the concept of geometrically necessary dislocations (Ashby, 1970) which accommodate plastic lattice bending and torsion. The link between the dislocation density tensor and the Cosserat curvature was pointed out by Günther (1958) and Kröner (1963). A micropolar crystal plasticity theory was developed by Forest et al. (1997, 2000). Extensions of this initial formulation have been proposed to include dislocation densities in (Mayeur et al., 2011; Mayeur and McDowell, 2014) and has been

combined with a gradient enhanced hardening law (Petryk and Stupkiewicz, 2016; Stupkiewicz and Petryk, 2016) by Rys et al. (2022). The application of Cosserat crystal plasticity to dynamic recrystallization has been considered by Blesgen (2017) in combination with a level-set approach to describe grain boundary motion. *Ad hoc* nucleation, however, was treated as usual. Finally, a continuum description of grain boundaries at the submicron scale has been proposed by Fressengeas et al. (2011); Taupin et al. (2013), which combines translational plastic incompatibility (dislocations) and rotational plastic incompatibility (disclinations) through the Cosserat moment of momentum balance. The KWC approach requires proper identification of the grain boundary energy and mobility functions from experimental measurements or molecular dynamics simulations as recently discussed by Ngenzi et al. (2021); Ngenzi and Queyreau (2023).

The aim of this work is to contribute to the mesoscopic and full-field simulation of the nucleation stage of recrystallization in single crystals. We emphasize that we are not proposing a new model for recrystallization, but rather demonstrate the capabilities of already existing frameworks, though combined with some novel grain boundary constitutive laws, to simulate spontaneous nucleation in single crystals . We will show through numerical simulations with the orientation phase field models (Kobayashi et al., 2000; Ask et al., 2018b) that lattice curvature in single crystals can lead to grain nucleation to accommodate these gradients. The process by which nucleation occurs in these cases is not related to SIBM or subgrain coarsening/coalescence but emerges as a consequence of the unstable development of strong lattice gradients inside grains. To our knowledge, these potentialities of KWC and KWC-Cosserat approaches have not been demonstrated in earlier contributions, although Admal et al. (2018) discussed subgrain nucleation due to plastic distortion within the framework of KWC-strain gradient plasticity. They open new perspectives in the simulation of recrystallization phenomena. No specific material is studied since non-dimensional equations and parameters are used but the ratio between parameters refer to copper at intermediate temperature, which is the targeted material in (Ask et al., 2018b, 2020).

The structure of this paper is as follows. The framework of orientation phase field models and Cosserat crystal plasticity is recalled in section 2. The stability of a uniform orientation gradient is studied by means of KWC finite element simulations in section 3. The impact of mechanics on grain nucleation is discussed in section 4 with special attention to skew-symmetric stresses building up inside diffuse grain boundaries. The role of stored energy induced by plastic deformation in the KWC model is assessed in 5. The final section 6 of this paper is devoted to the simulation of grain nucleation during torsion and annealing of a single crystal rod, as an application of the whole modeling and computational framework. The Appendix A is dedicated to the identification procedure of the used model parameters for copper as the targeted material. The asymptotic analysis of the KWC model performed by Lobkovsky and Warren (2001) is briefly recalled in Appendix B and details of the three-dimensional finite element implementation of the KWC-Cosserat model are given in Appendix C.

Notation

Vectors a_i are denoted by $\underline{\boldsymbol{a}}$. Second order tensors A_{ij} and fourth order tensors A_{ijkl} are represented by $\underset{\sim}{\boldsymbol{A}}$ and $\underset{\approx}{\boldsymbol{A}}$ respectively. The third order Levi-Civita tensor ϵ_{ijk} is written as $\underline{\underline{\boldsymbol{\epsilon}}}$. The simple contraction of two vectors $a_i b_i$ and two tensors $A_{ik}B_{kj}$ is denoted by $\underline{\boldsymbol{a}} \cdot \underline{\boldsymbol{b}}$ and $\underset{\sim}{\boldsymbol{A}} \cdot \underset{\sim}{\boldsymbol{B}}$. Double contraction of two tensors $A_{ij}B_{ij}$ is written as $\underset{\sim}{\boldsymbol{A}} : \underset{\sim}{\boldsymbol{B}}$. The dyadic product $A_{ij} = a_i b_j$ is indicated by $\underline{\boldsymbol{a}} \otimes \underline{\boldsymbol{b}}$. The notations $\underline{\boldsymbol{a}} \otimes \nabla$ and $\nabla \cdot \underline{\boldsymbol{a}}$ represent the gradient $\partial a_i/\partial x_j$ and divergence $\partial a_i/\partial x_i$ of a vector a_i. The divergence of a second order tensor $\partial A_{ij}/\partial x_j$ is denoted by $\underset{\sim}{\boldsymbol{A}} \cdot \nabla$. The symmetric and skew-symmetric parts of a second order tensor are given by:

$$\text{sym}(\underset{\sim}{\boldsymbol{A}}) = \frac{1}{2}\left(\underset{\sim}{\boldsymbol{A}} + \underset{\sim}{\boldsymbol{A}}^T\right), \quad \text{skew}(\underset{\sim}{\boldsymbol{A}}) = \frac{1}{2}\left(\underset{\sim}{\boldsymbol{A}} - \underset{\sim}{\boldsymbol{A}}^T\right) \tag{1}$$

The axial vector associated with a skew-symmetric second order $\underset{\sim}{\boldsymbol{A}}^{\text{skew}}$ is

$$\overset{\times}{\underline{\boldsymbol{A}}} = -\frac{1}{2}\underset{\approx}{\boldsymbol{\epsilon}} : \underset{\sim}{\boldsymbol{A}}^{\text{skew}}, \quad \underset{\sim}{\boldsymbol{A}}^{\text{skew}} = -\underset{\approx}{\boldsymbol{\epsilon}} \cdot \overset{\times}{\underline{\boldsymbol{A}}} \tag{2}$$

The continuum mechanical framework and its finite element implementation are limited to small strains, small rotations and curvatures, even though the finite deformation model formulation is available in (Ask et al., 2019).

2. Orientation phase fields models for microstructure evolution

2.1. Kobayashi-Warren-Carter phase field model

The two-dimensional phase field model proposed by Kobayashi et al. (2000); Warren et al. (2003) is based on two scalar order parameters: the crystal lattice orientation θ and the crystal order parameter ϕ. The latter varies between zero for a fully disordered phase and one for a perfect crystal. The presence of grain boundaries and defects such as dislocations locally contribute to lower the value of ϕ. The dimensionless free energy $\bar{\mathcal{F}}_{\text{KWC}}$ of a body $\bar{\Omega}$ for the KWC model is given by

$$\bar{\mathcal{F}}_{\text{KWC}} = \frac{\mathcal{F}_{\text{KWC}}}{f_0 \Lambda^3} = \int_{\bar{\Omega}} \bar{\psi}(\bar{\nabla}\theta, \phi, \bar{\nabla}\phi) + \phi \bar{E} d\bar{V} \tag{3}$$

where $\bar{E} = E/f_0$ is the dimensionless stored energy, f_0 [J/m^3] is a scaling factor for the magnitude of the free energy density and Λ [m] is a length scale, $\bar{\nabla} = \Lambda \nabla$ is the dimensionless gradient. The last term in Eq. (3) representing the stored energy contribution due to statistically stored dislocations, was introduced in the original KWC potential by Abrivard et al. (2012a). An alternative formulation of the stored energy potential in the context of KWC modeling can be found in (Takaki et al., 2008b). The dimensionless free energy density $\bar{\psi}(\bar{\nabla}\theta, \phi, \bar{\nabla}\phi)$ is independent of the lattice orientation due to the frame invariance requirement, and has the following form:

$$\bar{\psi}(\bar{\nabla}\theta, \phi, \bar{\nabla}\phi) = \psi(\nabla\theta, \phi, \nabla\phi)/f_0 = f(\phi) + \frac{\bar{\alpha}^2}{2}\left|\bar{\nabla}\phi\right|^2 + \bar{s} g(\phi)\left|\bar{\nabla}\theta\right| + \frac{\bar{\varepsilon}^2}{2} h(\phi)\left|\bar{\nabla}\theta\right|^2 \tag{4}$$

where the model parameters $\bar{\alpha} = \frac{\alpha}{\sqrt{f_0}\Lambda}, \bar{s} = \frac{s}{f_0 \Lambda}, \bar{\varepsilon} = \frac{\varepsilon}{\sqrt{f_0}\Lambda}$ are dimensionless. In addition to regular quadratic terms with respect to the gradient of the phase field variables, the singular term $|\bar{\nabla}\theta|$, not differentiable at 0, is required to localize grain boundaries of finite width. The term $|\bar{\nabla}\theta|^2$ is needed for grain boundary motion according to (Warren et al., 2003). The functions $f,\ g,\ h$ are dimensionless by construction and have the following form:

$$f(\phi) = \frac{1}{2}(1-\phi)^2 \tag{5}$$

$$g(\phi) = \phi^2 \quad \text{or} \quad g(\phi) = -2\left(\log(1-\phi) + \phi\right) \tag{6}$$

$$h(\phi) = \phi^2 \tag{7}$$

Note that two forms of the function $g(\phi)$ are employed. Using $g(\phi)$ as a logarithmic function, the Read-Shockley form of the grain boundary energy is recovered (Kobayashi et al., 2000). For $\phi = 1$ the logarithmic function $g(\phi)$ diverges, so that a regularization is needed for the numerical implementation of the model. This is achieved by adding a small positive constant $\gamma_g \ll 1$ to the argument of the logarithm.

A feature of the model is the presence of two interface widths, one for each phase field variable, as sketched in Fig. 1. The interface widths ℓ_ϕ and ℓ_θ of the phase fields ϕ and θ depend in a non-trivial way on the parameters $\bar{\alpha},\ \bar{s}$, and $\bar{\varepsilon}$. With the usual parameters used in the literature, l_ϕ can be almost one order of

magnitude larger than l_θ. In the matched asymptotics analysis performed by Lobkovsky and Warren (2001), the interface width ℓ_θ is defined as the region of non-zero orientation gradient in a bicrystal. Rather than adopting the usual definition $\ell_\phi = 2\bar{\alpha}$, we have chosen to take ℓ_θ and ℓ_ϕ as the distance between two points corresponding to 10% of the maximum value of the phase field gradients, in a simple one-dimensional case:

$$\ell_\theta = 2\bar{x} \mid \bar{x} > 0 \;\&\; |\bar{\nabla}\theta|(\bar{x}) = 0.1\max(|\bar{\nabla}\theta|) \tag{8}$$

$$\ell_\phi = 2\bar{x} \mid \bar{x} > 0 \;\&\; |\bar{\nabla}\phi|(\bar{x}) = 0.1\max(|\bar{\nabla}\phi|) \tag{9}$$

This definition has the advantage to better account for the large tails of the exponential profiles of the phase field, as shown in Fig. 1. The interface widths also depend on the misorientation angle, as shown in Fig. 2. At the mesoscale of a few micrometres, a typical interface width ℓ_θ can be selected down to a few hundred nanometers to remain in acceptable computational time. The difference between the interface widths can be mitigated somewhat by changing the magnitude of the contributions in the free energy density. This can be achieved by using the Modica-Mortola potential $f(\phi) = (1-\phi)^2/\bar{\alpha}$, as in (Giga et al., 2023). A finite element simulation using such a formulation of the KWC free energy was performed for a grain boundary energy comparable to that of the regular KWC model, and the resulting interface widths are plotted as well in Fig. 2 for a misorientation $\Delta\theta = 0.4$. It can be seen that the ratio ℓ_ϕ/ℓ_θ decreases from approximately 6 in the classical formulation to 4 in this modified version of the free energy.

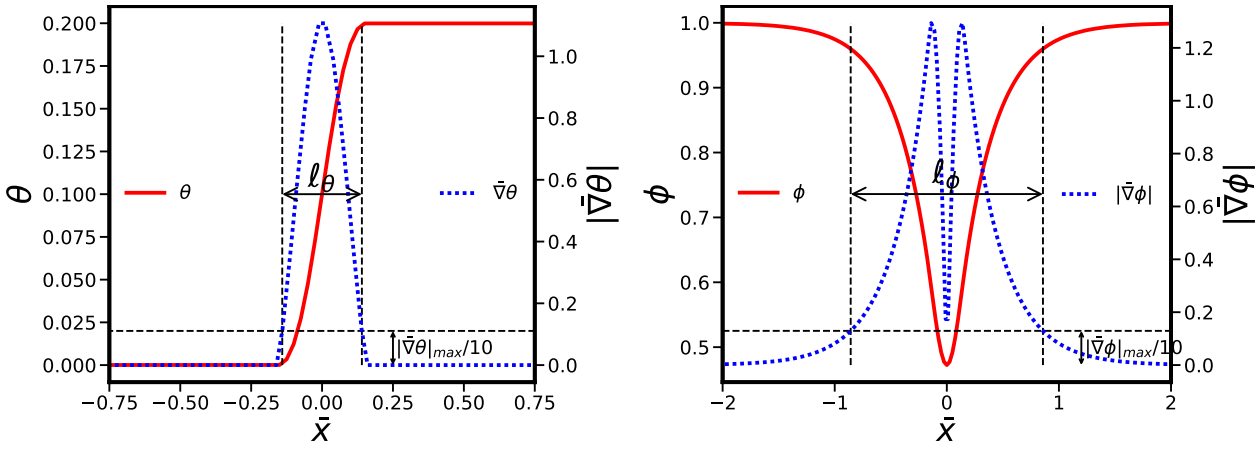

Fig. 1. Definition of the lengths ℓ_ϕ and ℓ_θ characterizing the width of the grain boundary zone.

Assuming relaxational dynamics for both phase fields, the evolution equations of the phase fields are given by

$$\bar{\eta}_\phi \dot{\phi} = \left(\frac{\partial\bar{\psi}}{\partial\bar{\nabla}\phi}\right)\cdot\bar{\nabla} - \frac{\partial\bar{\psi}}{\partial\phi} = \bar{\alpha}^2\bar{\nabla}^2\phi - f_{,\phi} - \bar{s}g_{,\phi}|\bar{\nabla}\theta| - \frac{\bar{\varepsilon}^2}{2}h_{,\phi}|\bar{\nabla}\theta|^2 - \bar{E} \tag{10}$$

$$P\bar{\eta}_\theta\phi^2\dot{\theta} = \left(\frac{\partial\bar{\psi}}{\partial\bar{\nabla}\theta}\right)\cdot\bar{\nabla} - \frac{\partial\bar{\psi}}{\partial\theta} = \bar{\nabla}\cdot\left(\bar{\varepsilon}^2 h\bar{\nabla}\theta + \bar{s}g\frac{\bar{\nabla}\theta}{|\bar{\nabla}\theta|}\right) \tag{11}$$

with $\dot{y} = \partial y/\partial\bar{t}, \quad \bar{t} = t/\tau_0$ where τ_0 is a time scale. P is a dimensionless inverse mobility function assumed to depend on ϕ and/or $\bar{\nabla}\theta$ and $\bar{\eta}_\phi$, $\bar{\eta}_\theta$ are constant kinetic factors. The choice $P = 1$ results in a spatially uniform mobility. Alternatively, the function P can be different in the bulk of the grain and in the diffuse grain boundary region to avoid simultaneous shrinkage and rotation during curvature driven migration by depending on $\bar{\nabla}\theta$:

$$P = 1 \quad \text{or} \quad P(\bar{\nabla}\theta) = 1 + \left(\frac{\bar{\mu}_p}{\bar{\varepsilon}} - 1\right)\exp\left(-\beta_p\bar{\varepsilon}|\bar{\nabla}\theta|\right) \tag{12}$$

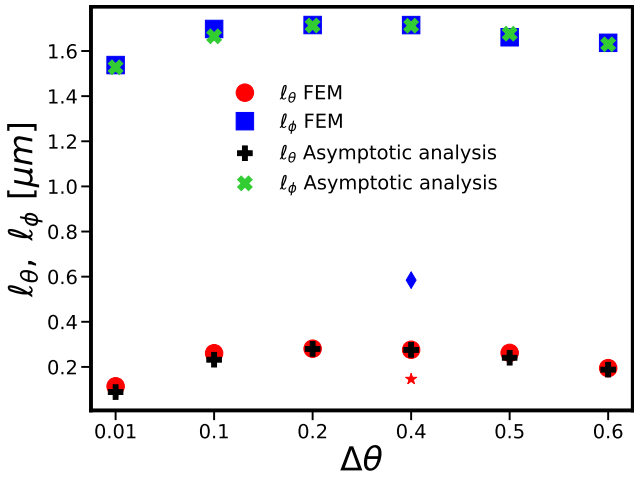

Fig. 2. Interface widths ℓ_ϕ and ℓ_θ as functions of misorientation $\Delta\theta$. The interface widths correspond to the distance between two points of 10% of the maximum of the phase field gradient. The additional star and diamond correspond to interface widths computed with a modified KWC free energy functional inspired from Giga et al. (2023).

A microforce formalism *á la* Gurtin (1996) provides a variational framework that allows to recover the evolution equations for the phase fields. For this purpose, internal microforces and microstress vectors $\bar{\pi}_\phi, \bar{\pi}_\theta, \underline{\bar{\boldsymbol{\xi}}}_\phi, \underline{\bar{\boldsymbol{\xi}}}_\theta$ are associated with $\phi, \theta, \bar{\nabla}\phi$ and $\bar{\nabla}\theta$ respectively. The application of the principle of virtual power gives the following balance equations in the body $\bar{\Omega}$ and boundary conditions on $\partial\bar{\Omega}$, here written in the absence of external and surface or volume densities of microforces:

$$\underline{\bar{\boldsymbol{\xi}}}_\phi \cdot \bar{\nabla} + \bar{\pi}_\phi^{sto} + \bar{\pi}_\phi^{dis} = 0 \quad \text{in } \bar{\Omega} \tag{13}$$

$$\underline{\bar{\boldsymbol{\xi}}}_\theta \cdot \bar{\nabla} + \bar{\pi}_\theta^{sto} + \bar{\pi}_\theta^{dis} = 0 \quad \text{in } \bar{\Omega} \tag{14}$$

$$\bar{\xi}_\phi \cdot \underline{\boldsymbol{n}} = 0, \quad \bar{\xi}_\theta \cdot \underline{\boldsymbol{n}} = 0 \quad \text{on } \partial\bar{\Omega} \tag{15}$$

with

$$\underline{\bar{\boldsymbol{\xi}}}_\phi = \frac{\partial\psi}{\partial\bar{\nabla}\phi}, \quad \underline{\bar{\boldsymbol{\xi}}}_\theta = \frac{\partial\psi}{\partial\bar{\nabla}\theta} \tag{16}$$

$$\bar{\pi}_\phi^{sto} = -\frac{\partial\psi}{\partial\phi}, \quad \bar{\pi}_\phi^{dis} = -\bar{\eta}_\phi\dot{\phi} \tag{17}$$

$$\bar{\pi}_\theta^{sto} = -\frac{\partial\psi}{\partial\theta}, \quad \bar{\pi}_\theta^{dis} = -\phi^2 P\bar{\eta}_\theta\dot{\theta} \tag{18}$$

so that the evolution equations (10)-(11) are retrieved.
An additional evolution equation for the stored energy must be added to account for recovery in the wake of the moving grain boundary. Following Abrivard et al. (2012a) the time evolution of the stored energy is given by:

$$\dot{\bar{E}} = \begin{cases} -C_D\bar{E}\tanh(\bar{C}_A|\bar{\nabla}\theta|^2)\dot{\phi}, & \dot{\phi} > 0 \\ 0, & \dot{\phi} \leq 0 \end{cases} \tag{19}$$

where C_D and $\bar{C}_A$ are constants settling the amplitude and rate of recovery. The singular term $1/|\bar{\nabla}\theta|$ in Eq. (11) requires regularization in the numerical treatment. In (Warren et al., 2003) this is achieved by replacing the term $|\bar{\nabla}\theta|$ in the free energy by a quadratic potential for orientation gradients below a numerical threshold

$1/\bar{\gamma}$:

$$|\bar{\nabla}\theta| \sim A_\gamma(|\bar{\nabla}\theta|) = \begin{cases} \frac{\bar{\gamma}}{2}|\bar{\nabla}\theta|^2 \text{ for } 0 \leq |\bar{\nabla}\theta| \leq 1/\bar{\gamma} \\ |\bar{\nabla}\theta| - \frac{1}{2\bar{\gamma}} \text{ for } |\bar{\nabla}\theta| > 1/\bar{\gamma} \end{cases} \tag{20}$$

The KWC model does not take mechanics into account and is therefore not sufficient in itself to model phenomena such as microstructural changes due to strain localization. The model developed by Ask et al. (2018b) proposes a unified framework based on continuum thermodynamics and consistently combines the KWC model with the Cosserat crystal plasticity theory of Forest et al. (1997).

2.2. Cosserat crystal plasticity

In a Cosserat continuum, a triad of non-deformable and orthonormal directors is attached to each material point. The medium is therefore endowed with the displacement vector $\underline{\boldsymbol{u}}$ and the independent microrotation axial vector $\underline{\boldsymbol{\theta}}$. In contrast to the KWC model of the previous section, the Cosserat model is formulated in the 3D case involving rotations represented by 3D axial vectors. The proposed model is formulated within the framework of small rotations, small strains and small curvatures. A small rotation is represented by an axial vector whose components can be interpreted as rotation angles with respect to the corresponding axes. Such an interpretation is wrong for finite rotations, for which indeed various alternative representations are available, such as quaternions or full rotation tensors. Within the framework of small rotations adopted in this paper, these representations are equivalent and the gradient of the axial vector coincides with the gradient of the rotation angles. At small deformation, rotation and curvature, the Cosserat microrotation tensor $\underset{\sim}{\boldsymbol{R}}$ is given by

$$\underset{\sim}{\boldsymbol{R}} = \underset{\sim}{\boldsymbol{I}} - \underline{\underline{\boldsymbol{\epsilon}}} \cdot \underline{\boldsymbol{\theta}} \tag{21}$$

where $\underset{\sim}{\boldsymbol{I}}$ is the second order identity tensor and $\underline{\underline{\boldsymbol{\epsilon}}}$ is the Levi-Civita permutation tensor. Within this framework, the deformation measures are the generally non-symmetric Cosserat deformation and curvature (or wryness) tensors $\underset{\sim}{\boldsymbol{e}}$ and $\underset{\sim}{\boldsymbol{\kappa}}$, respectively:

$$\underset{\sim}{\boldsymbol{e}} = \underline{\boldsymbol{u}} \otimes \nabla + \underline{\underline{\boldsymbol{\epsilon}}} \cdot \underline{\boldsymbol{\theta}} \tag{22}$$

$$\underset{\sim}{\boldsymbol{\kappa}} = \underline{\boldsymbol{\theta}} \otimes \nabla \tag{23}$$

The stress measures power-conjugate to the deformation rates are the force-stress tensor $\underset{\sim}{\boldsymbol{\sigma}}$ and the couple-stress tensor $\underset{\sim}{\boldsymbol{m}}$, which are also generally non-symmetric. They must satisfy the balance of momentum and balance of moment of momentum, recalled here in the static case and in the absence of volume forces and moments:

$$\underset{\sim}{\boldsymbol{\sigma}} \cdot \nabla = \underline{\boldsymbol{0}} \tag{24}$$

$$\underset{\sim}{\boldsymbol{m}} \cdot \nabla - \underline{\underline{\boldsymbol{\epsilon}}} : \underset{\sim}{\boldsymbol{\sigma}} = \underline{\boldsymbol{0}} \tag{25}$$

Equation (25) is similar to the KWC evolution equation for θ given by equation (11) where the term inside the brackets on the right hand side can be interpreted as a couple stress tensor $\underset{\sim}{\boldsymbol{m}}$.

The total strain tensor is additively decomposed into elastic and plastic contributions:

$$\underset{\sim}{\boldsymbol{e}} = \underset{\sim}{\boldsymbol{e}}^e + \underset{\sim}{\boldsymbol{e}}^p \tag{26}$$

The decomposition of the curvature tensor into plastic and elastic parts is considered for small and finite deformations respectively in Forest (1998); Forest et al. (1997) but it is assumed to be purely elastic in the present work for simplicity.

The classical free energy potential of a Cosserat continuum is based on quadratic contributions for both the strain and curvature tensors:

$$\psi(\underset{\sim}{\boldsymbol{e}}^e, \underset{\sim}{\boldsymbol{\kappa}}) = \frac{1}{2}\underset{\sim}{\boldsymbol{e}}^e : \underset{\approx}{\boldsymbol{E}} : \underset{\sim}{\boldsymbol{e}}^e + \frac{1}{2}\underset{\sim}{\boldsymbol{\kappa}} : \underset{\approx}{\boldsymbol{E}}^\kappa : \underset{\sim}{\boldsymbol{\kappa}} \tag{27}$$

where $\underset{\approx}{\boldsymbol{E}}$ and $\underset{\approx}{\boldsymbol{E}}^\kappa$ are fourth order tensors of elastic moduli. Extensions to rank-one and combined rank-one and quadratic contributions of the curvature tensor in the free energy have been considered by Forest and Ghiglione (2023).

In the isotropic case the constitutive equations are

$$\underset{\sim}{\boldsymbol{\sigma}} = \lambda \mathrm{Tr}\,(\underset{\sim}{\boldsymbol{e}}^e)\underset{\sim}{\boldsymbol{I}} + 2\mu \mathrm{sym}(\underset{\sim}{\boldsymbol{e}}^e) + 2\mu_c \mathrm{skew}(\underset{\sim}{\boldsymbol{e}}^e) \tag{28}$$

$$\underset{\sim}{\boldsymbol{m}} = \alpha \mathrm{Tr}\,(\kappa)\underset{\sim}{\boldsymbol{I}} + 2\beta \mathrm{sym}(\underset{\sim}{\boldsymbol{\kappa}}) + 2\gamma \mathrm{skew}(\underset{\sim}{\boldsymbol{\kappa}}) \tag{29}$$

where μ, λ are the Lamé coefficients and the parameters α, β, γ are the torsion-bending stiffnesses. The coupling modulus μ_c acts as a penalty parameter, forcing the Cosserat micro-rotation to follow the lattice rotation $\underset{\sim}{\boldsymbol{\omega}}^e$ according to (Ask et al., 2018b):

$$\underset{\sim}{\boldsymbol{\omega}}^e = \mathrm{skew}(\underset{\sim}{\boldsymbol{e}}^e) - \underline{\underline{\boldsymbol{\epsilon}}} \cdot \underline{\boldsymbol{\theta}} \tag{30}$$

By setting a sufficiently high μ_c, the skew-symmetric part of the elastic strain almost vanishes and the Cosserat micro-rotation becomes equal to the lattice rotation. The lattice curvature is then related to the dislocation density tensor $\underset{\sim}{\boldsymbol{\alpha}}$ by the following equation due to Nye (1953):

$$\underset{\sim}{\boldsymbol{\alpha}} \sim \underset{\sim}{\boldsymbol{\kappa}}^T - \mathrm{Tr}\,(\underset{\sim}{\boldsymbol{\kappa}})\underset{\sim}{\boldsymbol{I}} \tag{31}$$

The Cosserat curvature can therefore be interpreted as an approximate measure of the dislocation density tensor.

2.3. KWC-Cosserat model

In this section we briefly recall the coupled KWC-Cosserat model proposed by Ask et al. (2018a,b, 2020). This model is valid for small strains, rotations and curvatures and only considers the Read-Shockley part of the grain boundary energy-misoriation curve. It is therefore limited to relatively low angle grain boundaries. In contrast to the original KWC model, and in the same way as in the Cosserat model presented in the previous section, the coupled model is introduced in the full 3D case where the orientation is represented by the small axial vector $\underline{\boldsymbol{\theta}}$. This formulation couples the KWC phase field model to Cosserat mechanics via the following free energy potential:

$$\bar{\psi}(\phi, \bar{\nabla}\phi, \underline{\boldsymbol{\theta}} \otimes \bar{\nabla}, \underset{\sim}{\boldsymbol{e}}^e, \rho^\alpha) = \psi(\phi, \nabla\phi, \underline{\boldsymbol{\theta}} \otimes \nabla, \underset{\sim}{\boldsymbol{e}}^e, \rho^\alpha)/f_0 \tag{32}$$

$$= \underbrace{f(\phi) + \frac{\bar{\alpha}^2}{2}\left|\bar{\nabla}\phi\right|^2 + \bar{s}g(\phi)\|\underline{\boldsymbol{\theta}} \otimes \bar{\nabla}\| + \frac{\bar{\varepsilon}^2}{2}h(\phi)\|\underline{\boldsymbol{\theta}} \otimes \bar{\nabla}\|^2}_{\text{KWC GB energy}}$$

$$+ \underbrace{\frac{1}{2}\mathrm{sym}(\underset{\sim}{\boldsymbol{e}}^e) : \underset{\approx}{\bar{\boldsymbol{E}}}^s : \mathrm{sym}(\underset{\sim}{\boldsymbol{e}}^e) + 2\bar{\mu}_c \mathrm{skew}(\underset{\sim}{\boldsymbol{e}}^e) : \mathrm{skew}(\underset{\sim}{\boldsymbol{e}}^e)}_{\text{Cosserat strain energy}} + \underbrace{\bar{\psi}_\rho(\phi, \rho^\alpha)}_{\text{SSD accumulation}} \tag{33}$$

where the total elastic strain tensor has been split into two parts. The tensor $\underset{\approx}{\boldsymbol{E}}^s$ is the classical tensor of the elastic moduli acting on the symmetric elastic strain tensor, whereas $\bar{\mu}_c$ takes care of the skew-symmetric

deformation contribution. The stored energy potential, which takes into account the accumulation of statistically stored dislocations (SSD) is given by

$$\bar{\psi}_\rho(\phi, \rho^\alpha) = \frac{1}{2}\phi\bar{\mu}\bar{b}^2 \sum_{\alpha=1}^{N}\sum_{\beta=1}^{N} h^{\alpha\beta}\bar{\rho}^\beta \tag{34}$$

where $\mu, b, \rho^\alpha, h^{\alpha\beta}$ are respectively the shear modulus, the Burgers vector, the dislocation density of the slip system α and the slip system interaction matrix.

In this coupled formulation, the balance equations in the absence of external forces are then given by

$$\bar{\nabla}\cdot\bar{\underline{\boldsymbol{\xi}}}_\phi + \bar{\pi}_\phi^{sto} + \bar{\pi}_\phi^{dis} = 0 \qquad \text{in } \bar{\Omega} \tag{35}$$

$$\bar{\underset{\sim}{\boldsymbol{\sigma}}}\cdot\bar{\nabla} = 0 \qquad \text{in } \bar{\Omega} \tag{36}$$

$$\bar{\underset{\sim}{\boldsymbol{m}}}\cdot\bar{\nabla} + 2\overset{\times}{\bar{\underline{\boldsymbol{\sigma}}}} = 0 \qquad \text{in } \bar{\Omega} \tag{37}$$

The field equations are complemented by Neumann boundary conditions setting the values of the generalized fluxes $\bar{\underline{\boldsymbol{\xi}}}_\phi\cdot\underline{\boldsymbol{n}}, \bar{\underset{\sim}{\boldsymbol{\sigma}}}\cdot\underline{\boldsymbol{n}}, \bar{\underset{\sim}{\boldsymbol{m}}}\cdot\underline{\boldsymbol{n}}$ on $\partial\bar{\Omega}$.

The various stress measures satisfy the following constitutive equations, after derivation of the free energy potential (33):

$$\mathrm{sym}(\bar{\underset{\sim}{\boldsymbol{\sigma}}}) = \bar{\underset{\approx}{\boldsymbol{E}}}^s : \underset{\sim}{\boldsymbol{\varepsilon}}^e \tag{38}$$

$$\overset{\times}{\bar{\underline{\boldsymbol{\sigma}}}} = 2\bar{\mu}_c\overset{\times}{\underline{\boldsymbol{e}}}^{\,e} \tag{39}$$

$$\bar{\underset{\sim}{\boldsymbol{m}}} = \left[\bar{s}g(\phi)\frac{1}{\|\underline{\boldsymbol{\theta}}\otimes\bar{\nabla}\|} + \bar{\varepsilon}^2 h(\phi)\right]\underline{\boldsymbol{\theta}}\otimes\bar{\nabla} \tag{40}$$

$$\bar{\underline{\boldsymbol{\xi}}}_\phi = \bar{\alpha}^2\bar{\nabla}\phi \tag{41}$$

The inelastic strain rate given by the following Eq. (42) is assumed to have contributions from crystal plasticity in the bulk of the grain and viscoelastic/viscoplastic relaxation of the skew-symmetric stresses at the grain boundary in response to lattice reorientation:

$$\dot{\underset{\sim}{\boldsymbol{e}}}^{\,p} = \underbrace{\sum_{\alpha=1}^{N}\dot{\gamma}\,\underline{\boldsymbol{\ell}}^{\,\alpha}\otimes\underline{\boldsymbol{n}}^{\,\alpha}}_{\substack{\text{Crystal plasticity}\\ \text{in the bulk of the grain}}} - \underbrace{\underset{\sim}{\boldsymbol{\epsilon}}\cdot\dot{\underline{\boldsymbol{\theta}}}^{\star}}_{\substack{\text{Relaxation of skew-symmetric}\\ \text{stress at the GB}}} \tag{42}$$

where $\underline{\boldsymbol{\ell}}^{\,\alpha}$ and $\underline{\boldsymbol{n}}^{\,\alpha}$ are the slip direction and normal to the slip plane for the slip system α. The additional contribution to the classical crystal plasticity part is indeed necessary since during grain boundary migration, local lattice reorientation will occur inside the grain boundary and give rise to skew symmetric stresses, as shown by Eq. (39) combined with Eq. (30). This change of lattice orientation reference for a zero-stress state is represented by the axial vector $\underline{\boldsymbol{\theta}}^\star$, a grain boundary contribution to the skew symmetric part of the plastic deformation $\underset{\sim}{\boldsymbol{e}}^p$. In other words, in the bulk of the grain, lattice rotation is only due to elastic/plastic deformation, whereas in the grain boundary an orientation change is prompted by the evolution of $\underline{\boldsymbol{\theta}}^\star$, the orientation reference with zero skew-symmetric stress. This inelastic mechanism is associated with a relaxation equation whose driving force is the skew-symmetric stress. This constitutive equation is described in detail in section 4, where it is also shown that without this grain boundary relaxation, grain boundary motion would be hindered. Note that the quantities that appear in the constitutive laws and are defined in the crystal frame, such as the slip direction and normal to the slip plane in Eq. (42), are rotated based on

the rotation matrix associated with $\underline{\boldsymbol{\theta}}$. This means that the crystal orientation is updated at each material point/integration point.

The slip rate $\dot{\gamma}$ in Eq. (42) is given by the power law function:

$$\dot{\gamma} = \sum_{\alpha=1}^{N} \left\langle \frac{|\bar{\tau}^{\alpha}| - \bar{R}^{\alpha}}{\bar{K}} \right\rangle^{n} \text{sign}(\bar{\tau}^{\alpha}), \quad \bar{\tau}^{\alpha} = \bar{\underset{\sim}{\boldsymbol{\sigma}}} : \underline{\boldsymbol{\ell}}^{\alpha} \otimes \underline{\boldsymbol{n}}^{\alpha}, \quad \bar{R}^{\alpha} = \bar{\tau}_0 + \chi \bar{\mu} \bar{b} \sqrt{\sum_{\beta=1}^{N} h^{\alpha\beta} \bar{\rho}^{\beta}} \tag{43}$$

where $\langle \bullet \rangle = \max(0, \bullet)$, $\bar{K}, n$ are viscoplasticity parameters, and $\chi \sim 0.3$ is a coefficient. The resolved shear stress is denoted by $\bar{\tau}^{\alpha}$ and the critical resolved shear stress by $\bar{R}^{\alpha}$. The evolution of the SSD density follows a Kocks-Mecking law modified to account for static recovery in the wake of a moving grain boundary (Ask et al., 2020):

$$\dot{\bar{\rho}}^{\alpha} = \begin{cases} \dfrac{1}{\bar{b}} \left(\dfrac{1}{K_r} \sqrt{\sum_{\beta} \bar{\rho}^{\beta}} - 2\bar{d}\bar{\rho}^{\alpha} \right) |\dot{\gamma}^{\alpha}| \bar{\rho}^{\alpha} C_D \tanh\left(\bar{C}_A |\theta \otimes \bar{\nabla}| \right) \dot{\phi}, & \dot{\phi} > 0 \\ \dfrac{1}{\bar{b}} \left(\dfrac{1}{K_r} \sqrt{\sum_{\beta} \bar{\rho}^{\beta}} - 2\bar{d}\bar{\rho}^{\alpha} \right) |\dot{\gamma}^{\alpha}|, & \dot{\phi} \leq 0 \end{cases} \tag{44}$$

As a consequence of the introduction of the reference orientation $\underline{\boldsymbol{\theta}}^{\star}$ in Eq. (42) and of the presence of the penalty modulus $\bar{\mu}_c$, the skew-symmetric part of the elastic strain tensor is now given by

$$\overset{\times}{\underline{\boldsymbol{e}}}^{e} = \overset{\times}{\underline{\boldsymbol{\omega}}}^{e} - \underline{\boldsymbol{\theta}} - \underline{\boldsymbol{\theta}}^{\star} \simeq \underline{\mathbf{0}} \Rightarrow \overset{\times}{\underline{\boldsymbol{\omega}}}^{e} \simeq \underline{\boldsymbol{\theta}} + \underline{\boldsymbol{\theta}}^{\star} \tag{45}$$

As the Cosserat microrotation is associated with the lattice orientation, it is generally non-zero in the initial state. Thus, the reference configuration can be stress-free by setting proper initial conditions for the $\underline{\boldsymbol{\theta}}^{\star}$-field:

$$\underline{\boldsymbol{\theta}}^{\star}(t=0) = -\underline{\boldsymbol{\theta}}(t=0) \tag{46}$$

The inelastic grain boundary behavior is therefore necessary to accommodate an initial orientation distribution with a stress-free state. It can be seen as a reference orientation state of the grain, whose evolution law ensures that it is inherited to a region swept by a migrating grain boundary.

The finite element implementation of the presented models is based on the weak formulation of the balance laws. The discretization and resolution methods are described in the references (Abrivard et al., 2012a; Ask et al., 2018b) while details on the extension to the original 3D framework are given in Appendix C. The implicit finite element solver Z–set is used (Besson and Foerch, 1997; Z-set, 2022). Global resolution is carried out using a Newton-Raphson method and the nonlinear constitutive laws are time-integrated by means of a Runge-Kutta method with automatic time stepping, as described in (Besson et al., 2009).

3. Stability of an orientation gradient for the Kobayashi-Warren-Carter model

The stability of a prescribed lattice orientation gradient is investigated for the KWC model by means of quasi-1D finite element simulations. In this section, the stored energy $\bar{E}$ due to SSDs is zero in the crystal. Numerical experiments are carried out, in which the time evolution of the phase fields and key indicators are studied. The calculations are performed on a domain of total length $2\bar{L} = 20$ with one element in the height and 400 rectangular quadratic elements with reduced integration (8 nodes and 4 Gauss points) in the length.

The parameters used throughout are given in table 1 and correspond to pure copper at around 200 °C. The identification of these material parameters is detailed in Appendix A but a summary of the delicate procedure is given here. The parameters $\bar{\alpha}$, $\bar{s}$ are obtained by fitting the grain boundary energy-misorientation curve

on that of a $\langle 100 \rangle$ Cu tilt boundary (Wolf, 1990). The parameter $\bar{\varepsilon}$ controls the grain boundary width and is chosen in order that the grain boundary spans over a few finite element meshes to avoid pinning due to the discretization. With these parameters, the interface widths are typically $\ell_\phi \sim 1.6$ and $\ell_\theta \sim 0.3\,\mu\mathrm{m}$ (taking the normalizing distance $\Lambda = 1\,\mu\mathrm{m}$). The parameters $\bar{\mu}_p$ and β_p must be large enough to distinguish between the behavior in the bulk of the grain and at the grain boundary. Once these parameters are set, numerical experiments of stored energy driven migration are performed to determine the mobility coefficients $\bar{\eta}_\phi$ and $\bar{\eta}_\theta$. The resulting grain boundary mobility is then compared with the data measured by Vandermeer et al. (1997) to obtain a rough estimate of the temperature. The parameters γ and γ_g are appropriate regularization values for the rank one curvature term in the free energy density and logarithmic function $g(\phi)$ respectively.

Parameter	$\bar{\alpha}$	$\bar{s}$	$\bar{\varepsilon}$	$\bar{\eta}_\phi$	$\bar{\eta}_\theta$	$\bar{\mu}_p$	β_p	$\bar{\gamma}$	γ_g
Value	0.31	0.75	1	10	0.1	10^6	10^2	10^4	10^{-4}

Tab. 1. Model parameters used in the simulations with the KWC model.

3.1. Uniform orientation gradient

The first configuration considered is that of a spatially uniform initial orientation gradient in a single crystal. These initial conditions (IC) are summarized in the equation (47) with $\Delta\theta = 0.3$. Note that the initial uniform field $\phi = 1$ is not in equilibrium in the orientation gradient field. Dirichlet boundary conditions (BC) are imposed on the left and right boundaries of the domain for both ϕ and θ (equation (48)). This type of boundary condition for θ enforces the presence of a lattice orientation gradient from the left to the right. Multiple point constraints are also enforced at the top and bottom edges to ensure periodicity along the vertical direction (quasi-1D simulation).

$$\text{IC: } \begin{cases} \theta(\bar{t}=0,\bar{x}) = \Delta\theta \frac{\bar{x}+\bar{L}}{2\bar{L}} \\ \phi(\bar{t}=0,\bar{x}) = 1 \end{cases} \tag{47}$$

$$\text{BC: } \begin{cases} \theta(\bar{t},\bar{x}=-\bar{L}) = 0, \quad \theta(\bar{t},\bar{x}=\bar{L}) = \Delta\theta \\ \phi(\bar{t},\bar{x}=-\bar{L}) = \phi(\bar{t},\bar{x}=\bar{L}) = 1 \end{cases} \tag{48}$$

The profiles of ϕ and θ are plotted at different times in Fig. 3. First, as can be seen in Fig. 3a, the crystal order field reaches its equilibrium value around $\bar{t} = 100$ and grain boundaries begin to form near the left and right boundaries. At $\bar{t} = 350$, fluctuations of the order and orientation fields are observed in the linear central zone. These fluctuations reveal the unstable character of the linear orientation distribution. Next, the linear profile of the lattice orientation splits into a series of piece-wise constant regions that can be interpreted as subgrains with low angle grain boundaries. Initially, the distance between the neighboring grain boundaries is smaller than ℓ_ϕ. Consequently, the exponential tails of the phase field profiles of neighboring grains interact strongly and the subgrains merge to form grains with larger misorientations (Fig. 3c). The process evolves toward well separated grains will larger misorientations (Fig. 3d). The interfaces considered here are flat so that the observed migration of low angle grain boundaries is not due to GB curvature nor stored energy. The coalescence results from the overlap of the diffuse grain boundary regions of neighboring newly formed grains. Thus, the interface width ℓ_ϕ imposes a constraint on the maximum number of grains N that can be nucleated along the initial single crystal of total length $2\bar{L}$: $N < 2\bar{L}/\ell_\phi$.

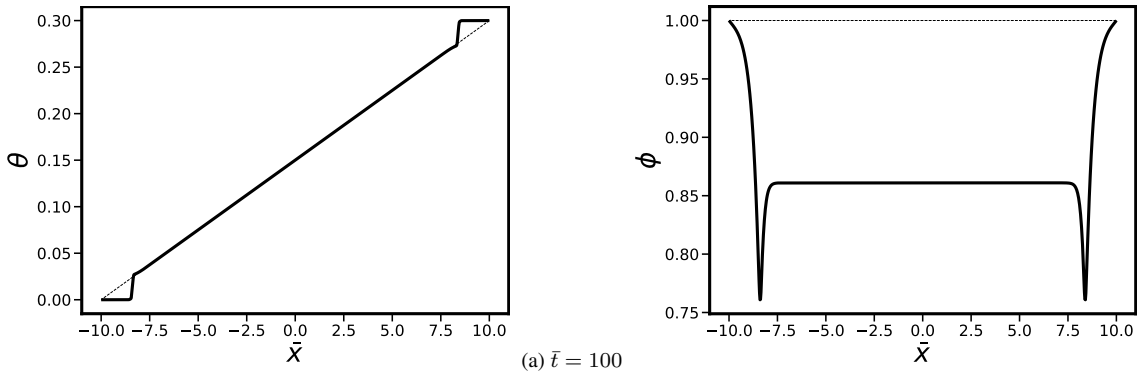

(a) $\bar{t} = 100$

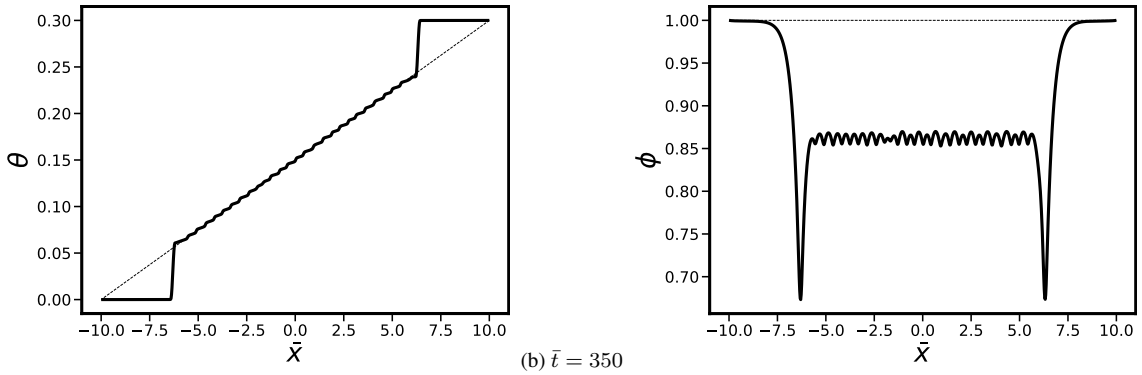

(b) $\bar{t} = 350$

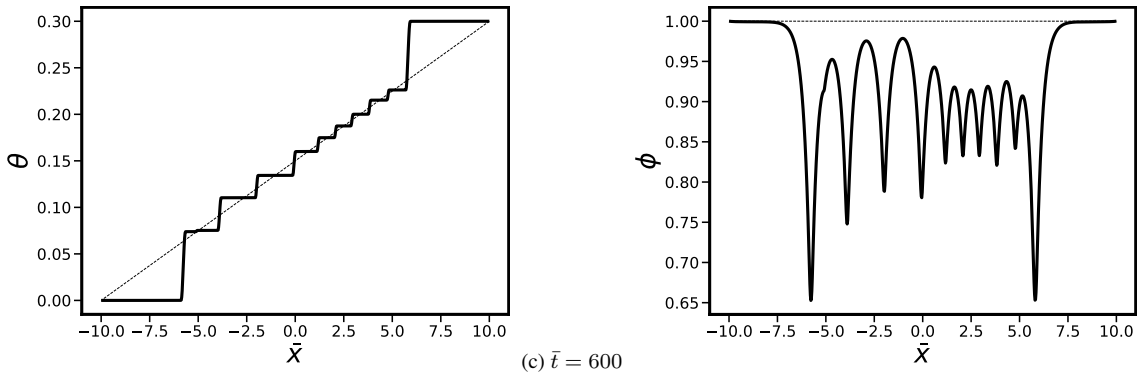

(c) $\bar{t} = 600$

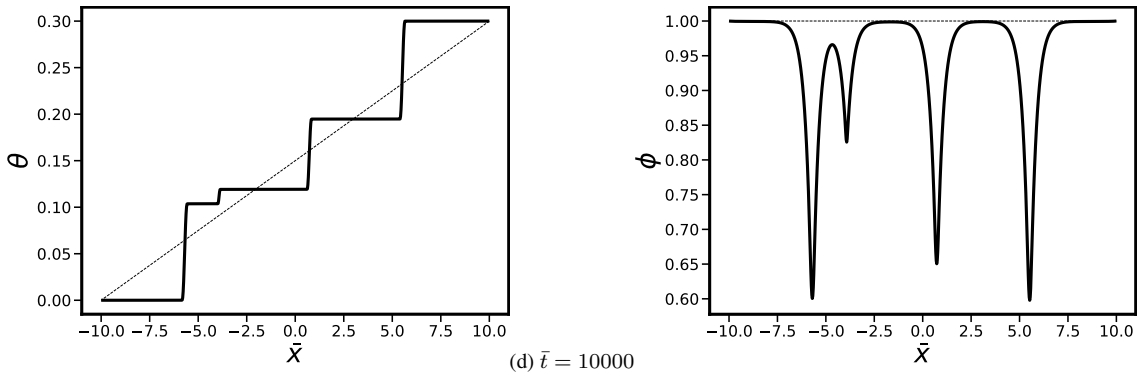

(d) $\bar{t} = 10000$

Fig. 3. Snapshots at different times $\bar{t}$ of the θ (left) and ϕ (right) profiles for a single crystal subjected to an initial uniform orientation gradient. The initial conditions are indicated by thin dashed lines.

To assess the existence of a threshold of orientation gradient to trigger nucleation in the KWC model, simulations were performed with different magnitudes of the orientation gradient $\Delta\theta \in \{0.01, 0.3, 0.6\}$. As can be seen in Fig. 4, it appears that (sub)grains are nucleated even for very low orientation gradients. Furthermore, as expected from the analysis in (Lobkovsky and Warren, 2001), the misorientation between grains as well as the minimum value of ϕ are found to depend on the value of the initial orientation gradient.

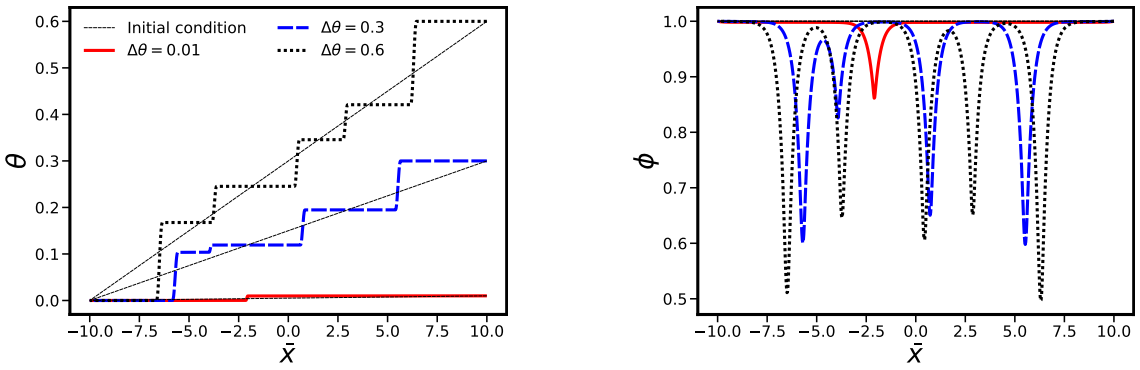

Fig. 4. Profiles of θ (left) and ϕ (right) at $\bar{t} = 10000$ for single crystals starting from initial homogeneous orientation gradients of different magnitudes.

3.2. Sinusoidal perturbation of the initial orientation gradient

The initial condition on the orientation field is now modified by adding a sinusoidal perturbation of spatial period $\bar{\lambda}$ and amplitude A:

$$\text{IC:} \begin{cases} \theta(\bar{t}=0,\bar{x}) = \Delta\theta \dfrac{\bar{x}+\bar{L}}{2\bar{L}} + A\sin\left(\dfrac{2\pi}{\bar{\lambda}}\bar{x}\right) \\ \phi(\bar{t}=0,\bar{x}) = 1 \end{cases} \tag{49}$$

Figure 5 shows the profiles of ϕ and θ for two values of the perturbation spatial period. It can be seen that the fluctuations of θ are captured by ϕ and the number of grains initially nucleated depends on $\bar{\lambda}$. However, the resulting microstructure exhibits overlapping diffuse grain boundaries that tend to coalesce. As in section 3.1 the width of the diffuse grain boundary zone for ϕ therefore sets a maximum value for the final number of grains.

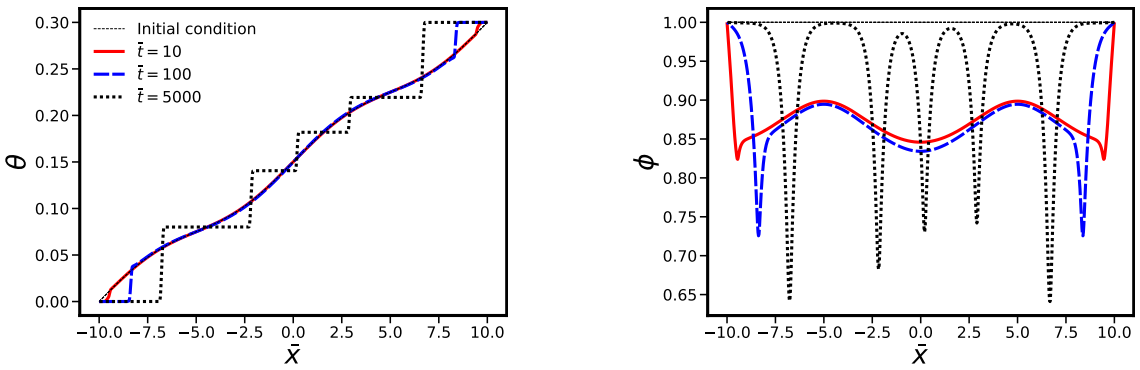

(a) $\bar{\lambda} = 10$

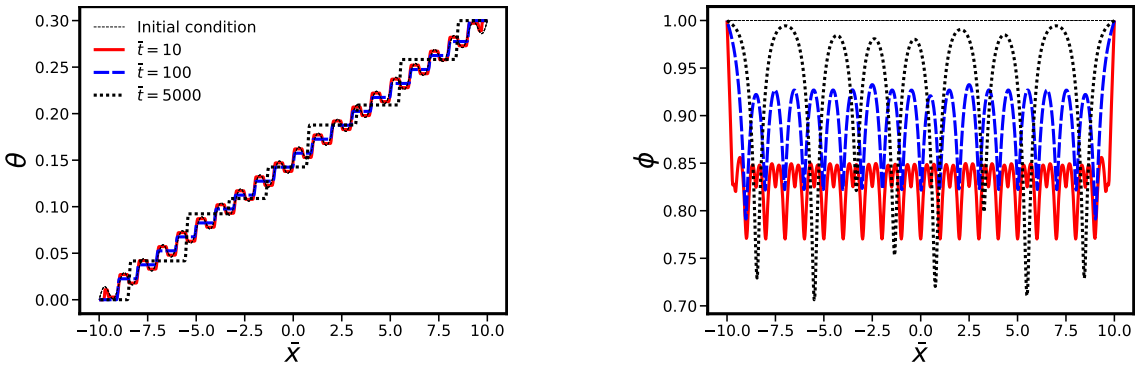

(b) $\bar{\lambda} = 1$

Fig. 5. Profiles of θ (left) and ϕ (right) for a single crystal starting from an initial orientation gradient with a sinusoidal perturbation of spatial period (a) $\bar{\lambda} = 10$, (b) $\bar{\lambda} = 1$ and amplitude $A = 0.01$.

3.3. Nucleation statistics

A study of the time evolution of the microstructure was carried out by following the evolution of indicators for $\bar{t} \in [0, 10^7]$ with data acquisition every 1000 increment of $\bar{t}$. At each time steps, we have collected the sets of values of (i) ϕ at the cusps defining the very center of the grain (sub-)boundaries, noted $\min(\phi)$; (ii) misorientation defined as the amplitude of the local jump of θ, noted $\Delta\theta$; (iii) the number and (iv) the size of the grains defined by the segments in the θ profiles where $\bar{\nabla}\theta$ is below 10^{-4}. The average, the minimum and the maximum in these sets are plotted in Fig. 6 with solid, blue and red lines respectively. The gray filling spans the interval [average $\pm$ standard deviation] for the considered quantity at time $\bar{t}$. Grains are defined as regions with uniform orientations. From Fig. 6a and 6b it is clear that the single crystal is rapidly fragmented into a large number of very small grains which then merge to form fewer and larger grains until only a bicrystal remains as $\bar{t} \to \infty$. This phenomenon is due to the Dirichlet boundary conditions which force the existence of a lattice orientation gradient. However, if zero flux boundary conditions were imposed for θ, the final state would be a single crystal, as this is the configuration with the lowest total energy due to the absence of interfaces. In Fig. 6c the minimum value of ϕ decreases globally as grains are merging, increasing the misorientation as seen in Fig. 6d. The peaks in the maximum value of $\min(\phi)$ (blue curve) are associated with these mergers: when two grains merge, the misorientation between them decreases, resulting in less deep ϕ cusps. As an example, a low angle GB between grain 2 and 3, starting from the left, can be observed in Fig. 3d (left). It is bound to vanish after sufficient time due to the interaction between the diffuse grain boundaries: as visible on the profile of ϕ there is no plateau, which is indicative of interacting fields. The configuration will therefore evolve towards a more stable one that comprises only three grains. Fig. 6a shows that the tricrystal is stable for a long time but is not the "final" configuration: with the KWC model, the final configuration is either a bicrystal or a single crystal, depending on the boundary conditions chosen for θ. If Dirichlet BC are applied, as done in the present example of Fig. 3d, then the final microstructure will be a bicrystal whose misorientation depends on the value of the BC. On the other hand, if zero flux BC are enforced the final configuration will be a single crystal. However, the plateaus of Fig. 6a indicate that grain distributions can be stable over long periods after the initial transient regime.

In the case of an initial uniform gradient of θ with a sine perturbation with period $\bar{\lambda} = 1$ and $\bar{\lambda} \to \infty$ (no perturbation), the time evolution of the total energy, computed numerically by integrating the free energy density over the whole domain, is also shown in Fig. 7. This confirms that the nucleation and merger processes due to orientation gradients lead to a global decrease in the total energy of the system. This is expected since the evolution equations of the KWC model are based on a minimization of the total energy. This also explains why, between $\bar{t} = 6 \times 10^5$ and $\bar{t} = 1.5 \times 10^6$, the tri-crystal slowly reorients towards the

more energetically favorable bicrystal. Note that energy of the final state corresponds to the grain boundary energy calculated with the matched asymptotics analysis of Lobkovsky and Warren (2001) that is briefly recalled in Appendix B.

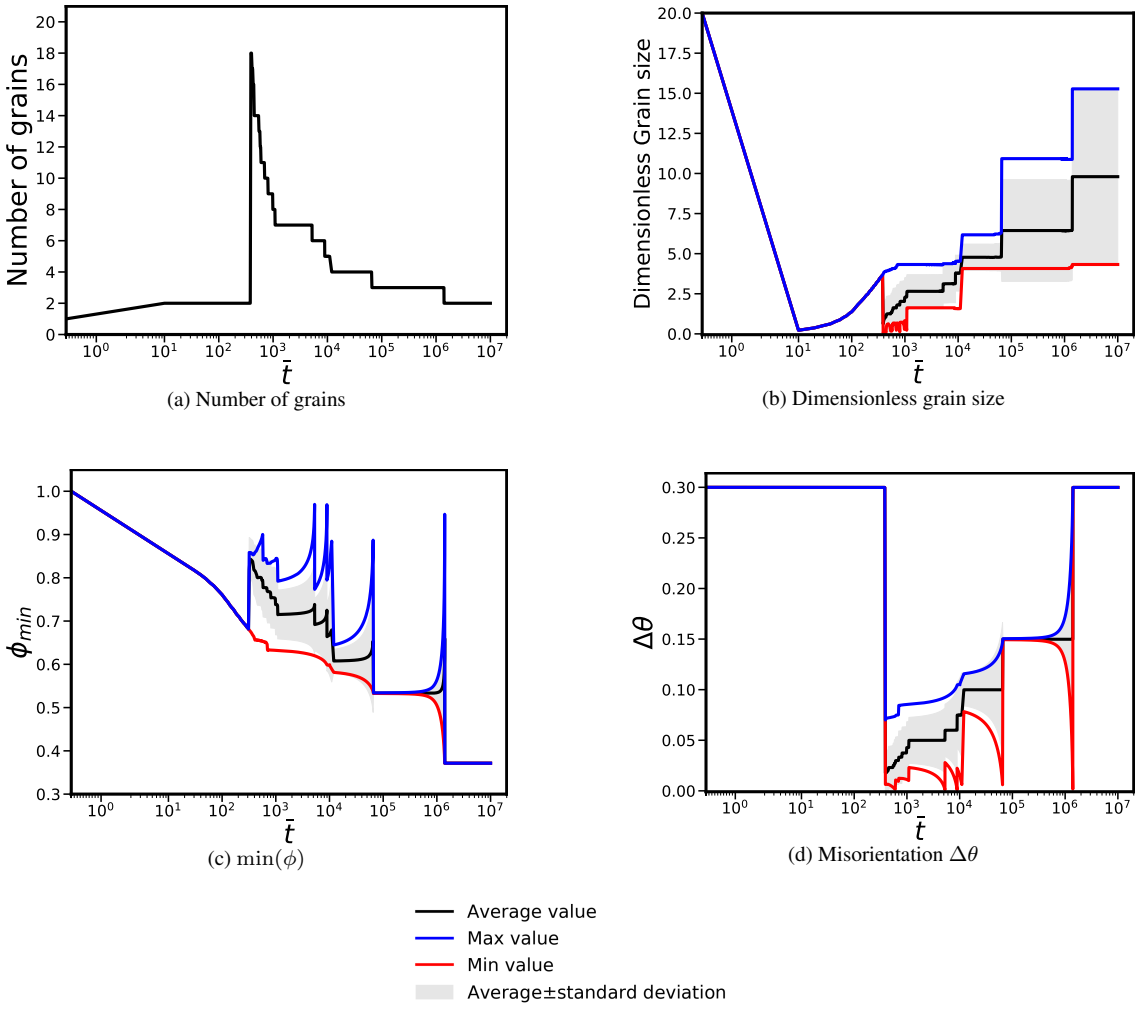

(a) Number of grains

(b) Dimensionless grain size

(c) $\min(\phi)$

(d) Misorientation $\Delta\theta$

Fig. 6. Time evolution of the number of grains (top left), dimensionless grain size (top right) as well as minimum value of ϕ (bottom left) and misorientation $\Delta\theta$ (bottom right) for a single crystal with initial homogeneous orientation gradient with the KWC model.

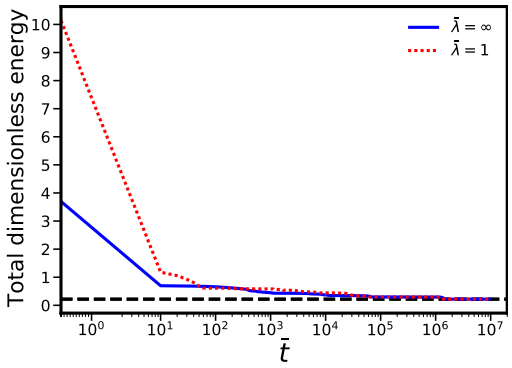

Fig. 7. Time evolution of the total dimensionless energy for a single crystal starting from a uniform orientation gradient perturbed by a sine with period $\bar{\lambda}$. The horizontal dashed line corresponds to the grain boundary energy of a bicrystal computed with the asymptotic analysis of Lobkovsky and Warren (2001).

4. Influence of mechanics on the stability of an orientation gradient

In this section, the previous stability problem is reconsidered to evaluate the effect of mechanics on the grain boundary formation. In the Cosserat-phase field model, stresses can develop in the diffuse grain boundary zones. Different formulations of the relaxation function are considered, namely a viscoelastic Maxwell model and a viscoplastic Norton law with threshold. These are illustrated in Fig. 8. The alternative Kelvin-Voigt model used in Ask et al. (2018b), also shown in Fig. 8, is not discussed in this paper. Finite element simulations are performed with the parameters given in table 2 on a regular two-dimensional domain of total length $2\bar{L} = 10$ with one element in height and 200 elements in length. This represents half of the region studied in the previous section, with the same element size, for saving computation time. Rectangular elements with quadratic shape functions with reduced integration are used. Only the viscoelastic and viscoplastic behavior of grain boundaries is considered in this section, which means that no dislocation slip is activated in the stability analysis. The material strip is not mechanically loaded, meaning that the prescribed mean stress is zero and that internal stresses can develop in the grain boundary regions.

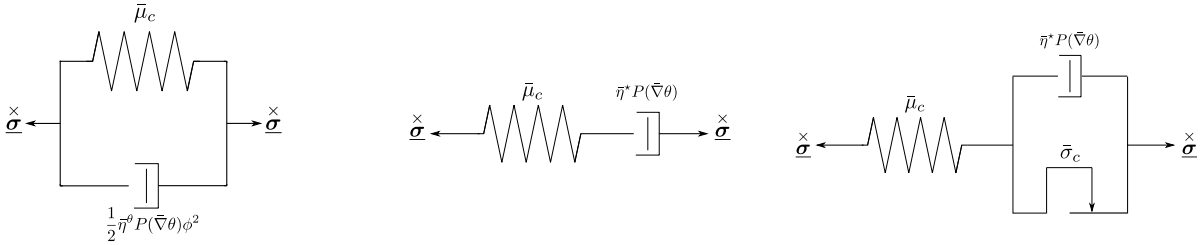

(a) Viscoelastic Kelvin-Voigt model used in Ask et al. (2018b,a).

(b) Viscoelastic Maxwell model used in Ask et al. (2020) and this work.

(c) Viscoplastic Norton model with threshold introduced in this work.

Fig. 8. Rheological models for relaxation of the skew-symmetric stresses in the diffuse grain boundaries.

Parameter	$\bar{E}^e$	ν	$\bar{\alpha}$	$\bar{s}$	$\bar{\varepsilon}$	$\bar{\eta}_\phi$	$\bar{\eta}^\star$	$\bar{\mu}_p$	β_p	$\bar{\gamma}$	γ_g
Value	56 000	0.3	0.31	0.75	1	10	1	10^6	10^3	10^4	10^{-4}

Tab. 2. Model parameters used in the simulations with the coupled model, in the absence of crystal plasticity.

4.1. Maxwell rheological model for the relaxation of the skew-symmetric stress

The first viscoelastic law considered is that of a Maxwell rheological model according to Ask et al. (2020). The evolution of the reference orientation is then given by

$$\dot{\underline{\boldsymbol{\theta}}}^{\star} = \frac{1}{\bar{\eta}^{\star} P(\bar{\nabla}\theta)} \overset{\times}{\bar{\boldsymbol{\sigma}}} = -\dot{\underline{\overset{\times}{\boldsymbol{e}}}}^{e} + \dot{\underline{\boldsymbol{\omega}}}^{e} - \dot{\underline{\boldsymbol{\theta}}} \tag{50}$$

where $\bar{\eta}^{\star}$ is a constant viscosity parameter and $P(\bar{\nabla}\theta)$ is the same function as in Eq. (12). Inserting Eq. (50) into the momentum balance (37) gives the following evolution for $\underline{\boldsymbol{\theta}}$:

$$\bar{\eta}^{\star} P(\bar{\nabla}\theta) \left[\dot{\underline{\overset{\times}{\boldsymbol{e}}}}^{e} - \dot{\underline{\overset{\times}{\boldsymbol{\omega}}}}^{e} + \dot{\underline{\boldsymbol{\theta}}} \right] = \left(\bar{s} g \frac{\underline{\boldsymbol{\theta}} \otimes \bar{\nabla}}{\|\underline{\boldsymbol{\theta}} \otimes \bar{\nabla}\|} + \frac{\bar{\varepsilon}^2}{2} h \|\underline{\boldsymbol{\theta}} \otimes \bar{\nabla}\| \right) \cdot \bar{\nabla} \tag{51}$$

The main difference from the original KWC evolution equation (11) is the addition of the relative rotation rate $\dot{\underline{\overset{\times}{\boldsymbol{e}}}}^{e} - \dot{\underline{\overset{\times}{\boldsymbol{\omega}}}}^{e}$ emerging from the mechanical coupling. Alternatively, a Kelvin-Voigt relaxation law has been used as in (Ask et al., 2018b). Note that, similarly to Ask et al. (2020) and unlike (Warren et al., 2003; Ask et al., 2018b), it was decided not to include the phenomenological coupling term ϕ^2 multiplying $P(\bar{\nabla}\theta)$, as it appeared to significantly increase the computational cost in the coupled model.

The following initial and boundary conditions are used to evaluate the effect of relaxation of the skew symmetric stress during grain boundary formation:

$$\text{IC: } \begin{cases} \phi(\bar{t}=0,\bar{x}) = 1 \\ \theta(\bar{t}=0,\bar{x}) = \frac{\Delta\theta}{2}(\tanh(15\bar{x})+1) \end{cases} \tag{52}$$

$$\text{BC: } \begin{cases} \phi(\bar{t},\bar{x}=-\bar{L}) = \phi(\bar{t},\bar{x}=\bar{L}) = 1 \\ \theta(\bar{t},\bar{x}=-\bar{L}) = 0, \quad \theta(\bar{t},\bar{x}=\bar{L}) = \Delta\theta \\ \bar{u}_x = \bar{u}_y = 0 \text{ at the bottom left corner} \\ \bar{u}_y = 0 \text{ at the top right corner} \end{cases} \tag{53}$$

with $\Delta\theta = 0.3$. Multiple point constraints are also imposed on the top and bottom edges to ensure the periodicity of $\phi, \theta, \bar{u}_x, \bar{u}_y$ along the vertical direction. The objective is to analyze the build-up and relaxation of stresses in the diffuse GB zone during the formation of a grain boundary. The out-of-equilibrium initial conditions lead to instantaneous build-up of stresses in the GB region which then relax according to the viscoelastic law for $\theta^{\star}$. The results of the simulation are shown in Fig. 9, which shows the element-averaged profiles of $\text{sym}(\bar{\underset{\sim}{\boldsymbol{\sigma}}})_{12}$ and $\overset{\times}{\bar{\sigma}} = \text{skew}(\bar{\underset{\sim}{\boldsymbol{\sigma}}})_{12}$ at different times during the grain boundary formation. The stresses $\text{sym}(\bar{\underset{\sim}{\boldsymbol{\sigma}}})_{12}$ and $\text{skew}(\bar{\underset{\sim}{\boldsymbol{\sigma}}})_{12}$ are clearly mirror images of each other with respect to the line $\bar{y}=0$ and the profiles are also antisymmetric with respect to $\bar{x}=0$. The stresses vanish in the region where $|\bar{\nabla}\theta| \neq 0$, as expected from the localization function $P(\bar{\nabla}\theta)$. Numerical residual stresses of the order of 10^{-2} are present after full relaxation.

The existence of internal stresses in the grain boundary region is a physically relevant feature due to strong elastic strains induced by change of atomic order. Such nanoscale residual stresses can be computed by molecular dynamics but also continuum theories. Interestingly, the profile of $\text{sym}(\bar{\underset{\sim}{\boldsymbol{\sigma}}})_{12}$ resembles that of the elasto-plastic theory of dislocation and disclination fields by Taupin et al. (2013), as shown in Fig. 10, probably because they both share the same generalized balance equation for the moment of momentum and associated couple stress tensor. It can be seen that they show similar trends, such as sharp variation in a narrow region and anti-symmetric profile. However, a major difference is that in the nanoscale model of Taupin et al. (2013) a residual stress still remains *within* the grain boundary at equilibrium, whereas in the micron-scale model of Ask et al. (2020) relaxed grain boundaries are assumed to be stress-free and only

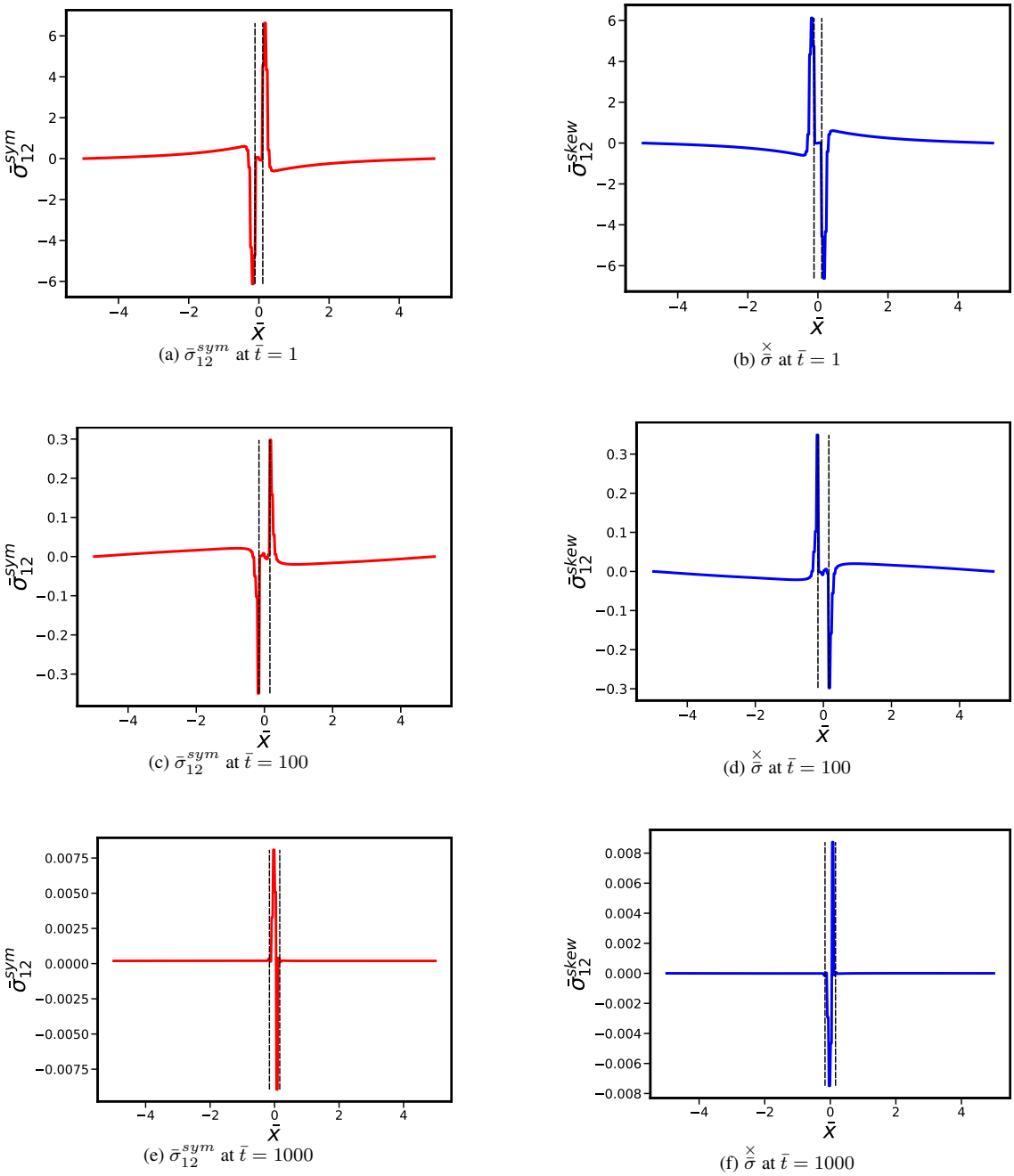

(a) $\bar{\sigma}_{12}^{sym}$ at $\bar{t} = 1$

(b) $\overset{\times}{\bar{\sigma}}$ at $\bar{t} = 1$

(c) $\bar{\sigma}_{12}^{sym}$ at $\bar{t} = 100$

(d) $\overset{\times}{\bar{\sigma}}$ at $\bar{t} = 100$

(e) $\bar{\sigma}_{12}^{sym}$ at $\bar{t} = 1000$

(f) $\overset{\times}{\bar{\sigma}}$ at $\bar{t} = 1000$

Fig. 9. Relaxation of the element averaged symmetric shear stress component $\bar{\sigma}_{12}^{sym}$ (in red on the left) and skew-symmetric shear stress $\overset{\times}{\bar{\sigma}}$ (in blue on the right) for the KWC-Cosserat model with Maxwell type relaxation during grain boundary formation. The vertical dashed lines mark the region where $|\bar{\nabla}\theta| \neq 0$.

transient stresses are observed. Nevertheless, these residual stresses can play some role in the GB formation and migration. That is why a viscoplastic formulation of the GB behavior including a threshold is introduced in the next section.

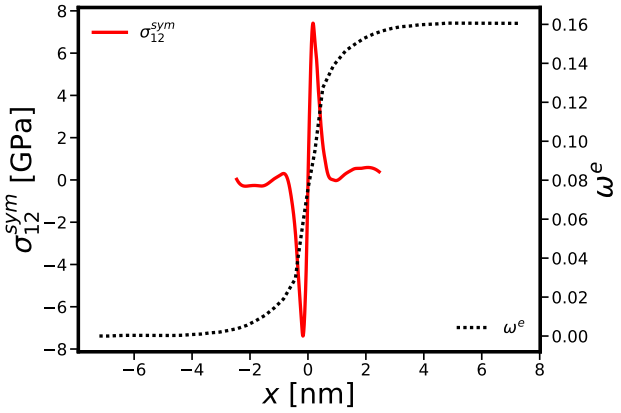

(a) Stress profile of σ_{12}^{sym} and compatible lattice rotation ω^e (relative to $36.87°$) along a relaxed $< 001 > \Sigma 29(520)$ tilt boundary of misorientation $46.40°$ after Taupin et al. (2013).

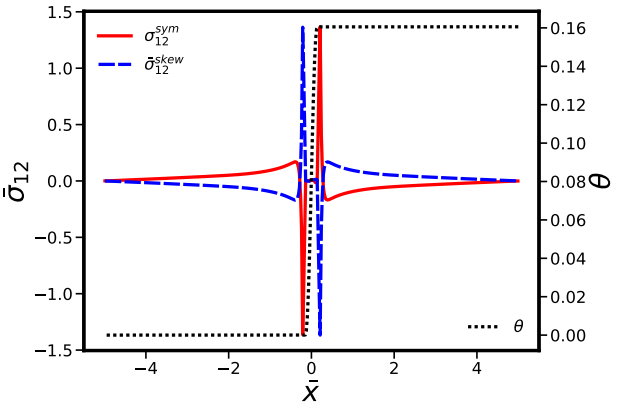

(b) Stress profiles of σ_{12}^{sym}, σ_{12}^{skew} and microrotation θ at $\bar{t} = 31$ along a bicrystal of misorientation $9.2°$. The stresses are not fully relaxed.

Fig. 10. Superimposed stress and rotation profiles for a grain boundary according to Taupin et al. (2013) (left) and using the KWC-Cosserat model of Ask et al. (2020) (right).

4.2. Introduction of a threshold: residual skew-symmetric stresses

The second relaxation law considered in this paper is based on a Norton formulation with threshold, which gives the following evolution for $\dot{\underline{\boldsymbol{\theta}}}^{\star}$:

$$\dot{\underline{\boldsymbol{\theta}}}^{\star} = \frac{1}{\bar{\eta}^{\star} P(\theta \otimes \bar{\nabla})} \left\langle \frac{|\overset{\times}{\underline{\boldsymbol{\sigma}}}| - \bar{\sigma}_c}{\bar{K}_c} \right\rangle^{n_c} \frac{\overset{\times}{\underline{\boldsymbol{\sigma}}}}{|\overset{\times}{\underline{\boldsymbol{\sigma}}}|} \tag{54}$$

where $\bar{\sigma}_c$ is the stress threshold for relaxation and $\bar{K}_c, n_c$ are viscoplasticity type parameters. In the following, the two-dimensional case is considered with $\bar{K}_c = n_c = 1$, so that

$$\dot{\theta}^{\star} = \frac{1}{\bar{\eta}^{\star} P(\bar{\nabla}\theta)} \left\langle |\overset{\times}{\bar{\sigma}}| - \bar{\sigma}_c \right\rangle \mathrm{sgn}(\overset{\times}{\bar{\sigma}}) \tag{55}$$

The influence of the value of the stress threshold $\bar{\sigma}_c$ on the profiles of ϕ and θ during grain boundary formation is shown in Fig. 11. As $\bar{\sigma}_c \to 0$ the behavior of the Maxwell relaxation model is recovered and the profiles are identical to the original KWC model. However, increasing the threshold leads to a delay in the development of the equilibrium profiles.

The effect of the threshold on the stress profile of $\mathrm{skew}(\bar{\underset{\sim}{\boldsymbol{\sigma}}})_{12}$ is illustrated in Fig. 12. Fluctuations of stresses are observed in the GB zone at the initial stage due to the strong out-of-equilibrium initial conditions. At the point of maximum relaxation ($\bar{t} = 1000$), all stresses above the threshold have decreased to the value of $\bar{\sigma}_c$, forming plateau-like regions. The stresses below this value are not relaxed, which explains why some oscillations below $\bar{\sigma}_c$ still remain. The introduction of a viscoplastic GB law with threshold enables therefore the existence of residual stresses in the GB region.

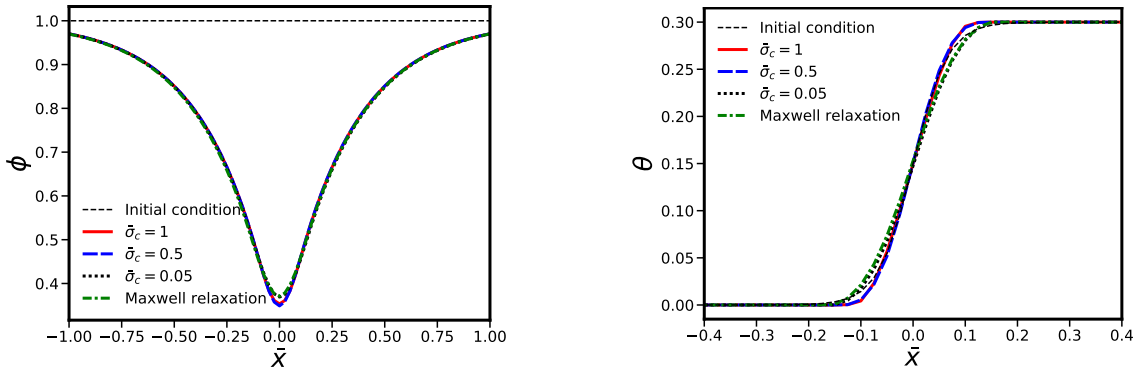

Fig. 11. Influence of the magnitude of the critical skew-symmetric stress in the KWC-Cosserat model with Norton law with threshold on the profiles of ϕ and θ at $\bar{t} = 200$ during grain boundary formation.

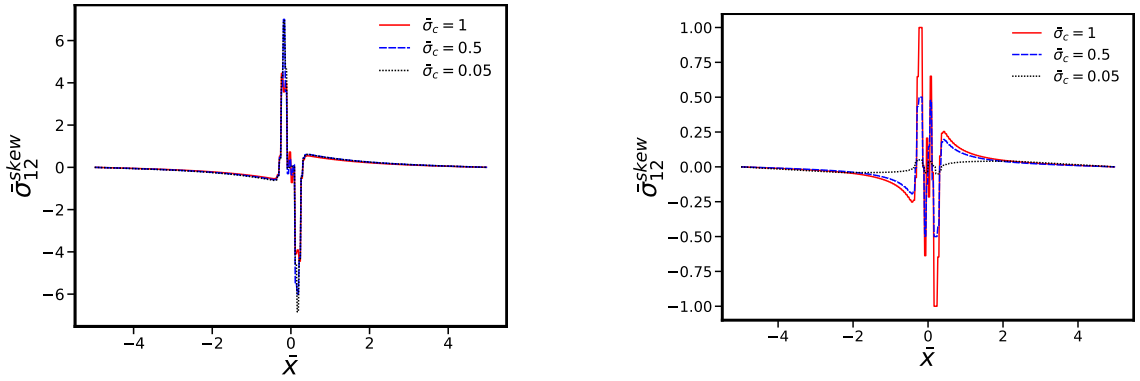

(a) $\bar{t} = 1$ (b) $\bar{t} = 1000$

Fig. 12. Relaxation of the skew-symmetric stress for the KWC-Cosserat model with Norton relaxation law with threshold during grain boundary formation.

4.3. Grain nucleation in the KWC-Cosserat medium in the absence of crystal plasticity

The stability analysis of section 3.2 is revisited by including mechanical aspects in the problem, in particular the effect of skew-symmetric stresses. The nucleation behavior of the KWC-Cosserat model is assessed here for a single crystal subjected to a uniform orientation gradient. A first simulation is run with the KWC model to determine the equilibrium profile of ϕ with respect to the initial orientation field by imposing a linear θ. The obtained fields then serve as initial conditions in subsequent computations in order to limit oscillations caused by too far from equilibrium initial conditions. Then the stability of a uniform orientation gradient is investigated again by adding elastic and viscoelastic/viscoplastic effects in the grain boundaries with Young's modulus $E^e = 130$ GPa and Poisson's ratio $\nu = 0.3$. For the Maxwell relaxation law, no significant differences are observed with regards to the original KWC model, as shown in Fig. 13a. When a Norton relaxation model with threshold is chosen, the existence of the yield stress can substantially delay grain boundary nucleation as shown in Fig.13b. For example, for a value of $\bar{\sigma}_c = 0.5$ or $\bar{\sigma}_c = 0.25$ the nucleation process is still in its early stages at $\bar{t} = 1000$ as the profiles in the central zone away from the left and right boundaries of the domain are the same as the initial conditions. In comparison, lower values of the threshold, such as $\bar{\sigma}_c = 0.05$, allow nucleation to occur at the same $\bar{t}$. As expected, for $\bar{\sigma}_c \to 0$ the behavior is similar to the KWC model. The introduction of residual stresses can therefore delay or even impede the GB formation and migration.

When using the coupled model, the final microstructure will depend on the presence of residual stresses: when total stress relaxation is allowed (i.e without a threshold) the expected stable configuration as $\bar{t} \to \infty$ is

either a single crystal or a bicrystal, possibly after (unrealistically) long time depending on the configuration. However, when there is a threshold that only allows partial stress relaxation, the presence of residual stresses will delay or even prevent further microstructure evolution. To this end, the threshold must initially be low enough to allow nucleation to occur within a reasonable time, and the "locking" of certain configurations becomes possible.

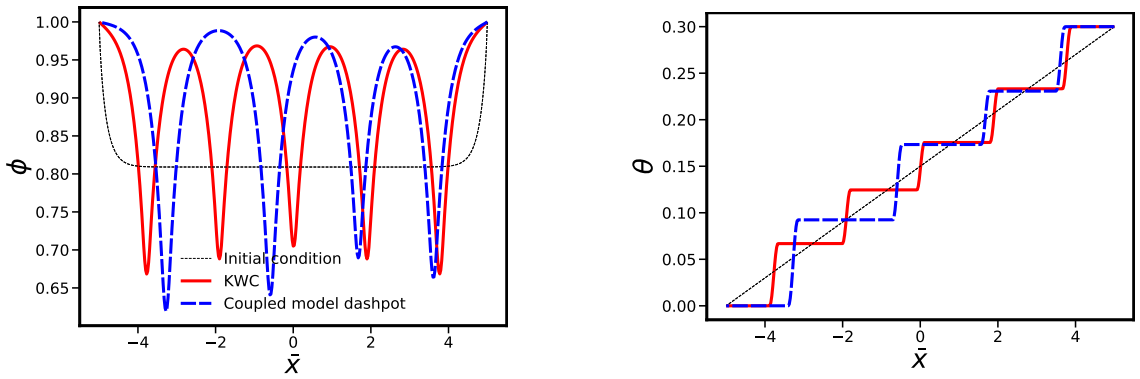

(a) KWC-Cosserat model with Maxwell relaxation law.

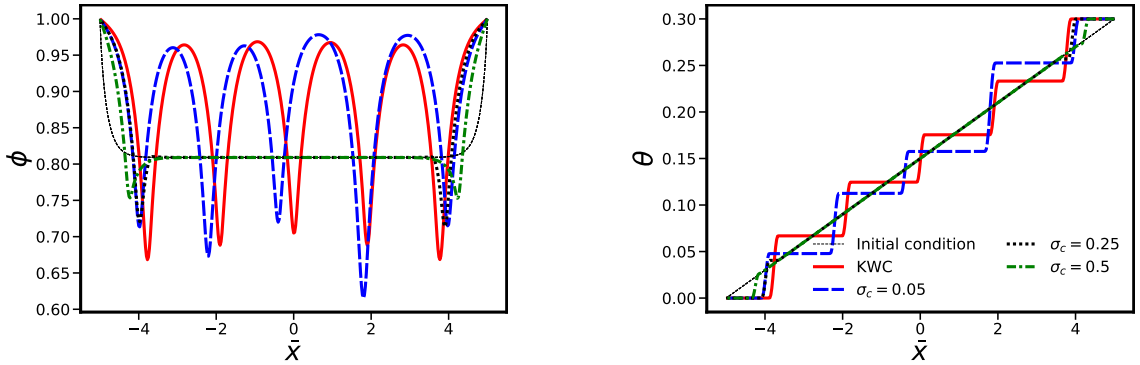

(b) KWC-Cosserat model with Norton GB relaxation law with threshold.

Fig. 13. Profiles of ϕ (left) and θ (right) at $\bar{t} = 1000$ for a single crystal with a uniform initial orientation gradient for the KWC-Cosserat model with Maxwell relaxation law (top) and Norton law with threshold (bottom).

5. Gradient of stored energy

Elastic energy can be stored by dislocations in the absence of orientation gradient as a result of plasticity induced dislocation multiplication and accumulation (SSDs), see Abrivard et al. (2012b). A Gradient of stored energy $\bar{E}$ is known to promote GB migration. In this section, we first study the influence of mechanics on the stored energy driven migration of a flat interface and then investigate the stability of such a gradient in the KWC-Cosserat medium. In the latter study, the initial crystal orientation is assumed to be homogeneous. Simultaneous gradients of orientation and stored energy $\bar{E}$ are then considered. The parameters given in table 2 are used in all the simulations with $C_D = 100$ and $\bar{C}_A = 1$ to account for full recovery behind the moving grain boundary.

5.1. Stored energy driven grain boundary migration in a 1D bicrystal

The energy coming from the accumulation of SSD provides an important driving force for grain boundary migration and recrystallization. Stored energy $\bar{E}$ was introduced in the KWC model by Abrivard et al. (2012a) where it was shown that the order parameter is modified by the presence of stored energy and reaches the following value at equilibrium:

$$\phi_{eq} = 1 - \bar{E} \tag{56}$$

Simulations of stored energy driven migration are performed in a bicrystal by prescribing an initial heterogeneous stored energy distribution: $\bar{E} = 0.01$ on the left side of the grain boundary and $\bar{E} = 0.1$ on its right side. A first preliminary computation is performed with the KWC model to find the equilibrium profiles of ϕ and θ. In a second time, the symmetric and skew-symmetric stresses are relaxed by the KWC-Cosserat model with the Maxwell GB model. The resulting ϕ, θ and $\bar{E}$ fields then serve as initial conditions for the simulation of stored energy-driven migration in a bicrystal. Figure 14 shows ϕ and θ at $\bar{t} = 400$ for the original KWC model and the two versions of the KWC-Cosserat model presented above. Comparing the KWC-Cosserat model with Maxwell's relaxation law and the original KWC model, the differences in the observed kinetics are due to the dissimilar evolution equations for θ, Eq. (11) and (51). For the KWC-Cosserat model with threshold, increasing the magnitude of $\bar{\sigma}_c$ slows down the grain boundary motion and can even pin it if it is high enough. Pinning of the grain boundary is observed here for $\bar{\sigma}_c = 0.5$ but this property will depend in general on the ratio between the values of the stored energy jump and GB yielding threshold.

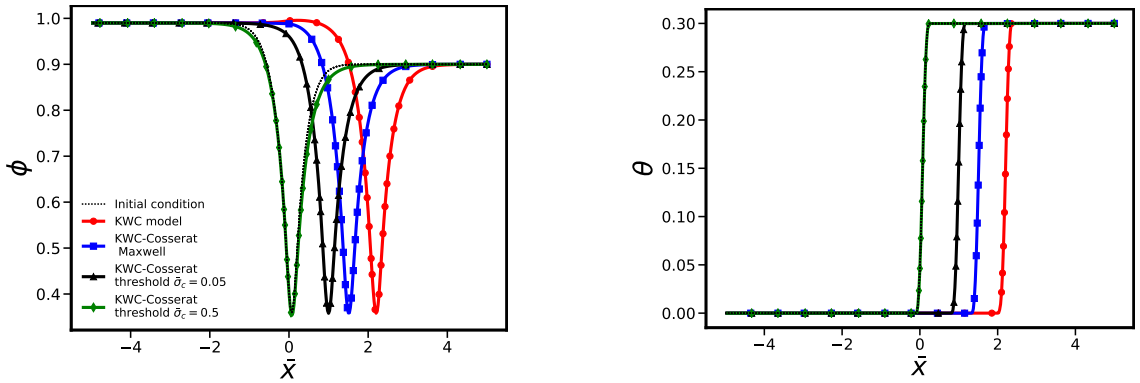

Fig. 14. Comparison of the KWC and KWC-Cosserat model with different GB relaxation laws for the stored energy driven migration of a flat interface. The profiles of ϕ (on the left) and θ (on the right) are plotted at $\bar{t} = 400$.

5.2. *Stability of an SSD density gradient*

Similar to section 3, the effect of a constant SSD-based stored energy gradient on nucleation is studied with the original KWC model. For that purpose, a linear profile of slope $\Delta\bar{E}$ is prescribed in a single crystal with uniform lattice orientation. Zero flux boundary conditions are applied for both ϕ and θ. As shown in Fig. 15, no grain has been formed and ϕ simply follows equation (56) away from the domain boundaries where the boundary conditions impose $\bar{\nabla}\phi \cdot \underline{\boldsymbol{n}} = 0$, $\underline{\boldsymbol{n}}$ being the outward normal vector. The lattice orientation remains uniform and equal to its initial value, meaning that a decrease in the crystal order due to the presence of defects (here the SSD) does not lead to a lattice reorientation.

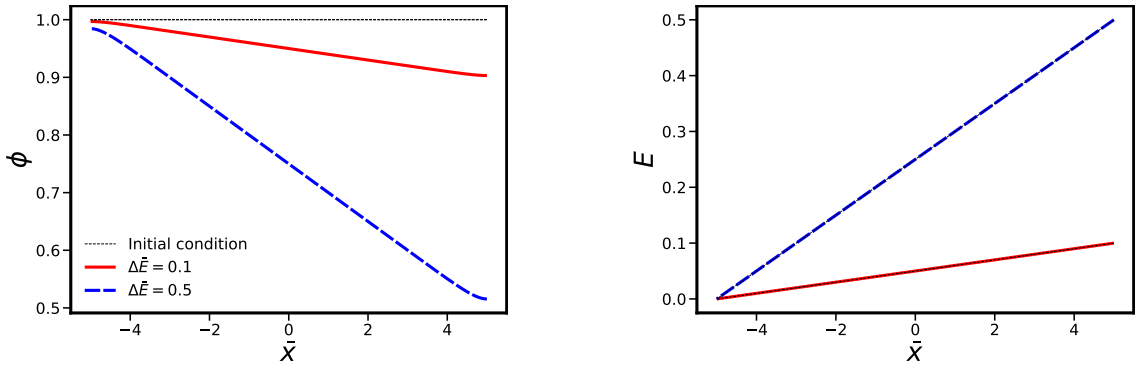

Fig. 15. Profiles of ϕ (left) and $\bar{E}$ (right) for a single crystal starting from uniform gradients of stored energy of different magnitudes. The orientation θ is uniform and equal to 0. The simulations are performed with the KWC model.

5.3. *Stability of superimposed SSD and GND density gradients*

Now combining uniform initial gradients of both orientation and stored energy, the former triggers grain nucleation whereas the latter provides a driving force for grain boundary motion. Figure 16 shows such simulations with the KWC model comparing the influence of the magnitude of the stored energy gradient on the resulting microstructure. During the early stages of nucleation, when grain boundaries are not well resolved, the stored energy influences the dynamics of the fluctuations. Therefore the subsequent merging of neighboring grains is different from the previous calculations without stored energy, as illustrated by the difference in the profiles of ϕ in Fig. 16a at $\bar{t} = 51$. At a later stage, when the grain boundaries are better established, merger of neighboring grains is promoted by the grain boundary motion induced by the stored energy. Such a phenomenon can be seen in Figs. 16c-16b, where the grain boundaries at $\bar{x} = -2.8$ and $\bar{x} = -1.1$ at $\bar{t} = 51$ have merged. The fact that migration occurred in part due to stored energy is evident in the stored energy profile of Fig. 16b, as a decrease in stored energy indicates recovery in the wake of the moving grain boundary. These figures also show stored energy driven migration without grain coalescence, as the grain boundary located at $\bar{x} = 1.6$ has moved to the boundary of the domain at $\bar{t} = 2001$.

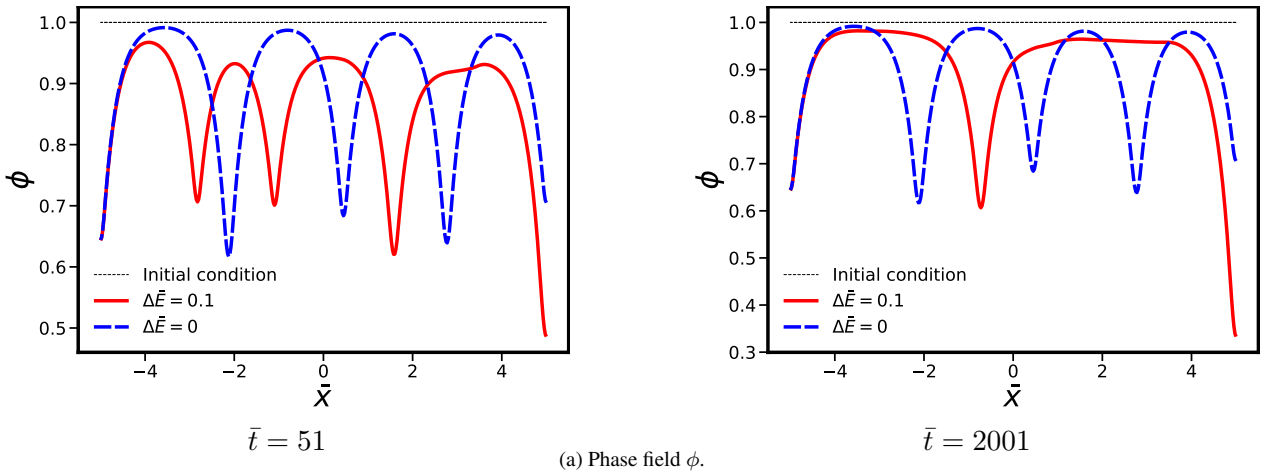

(a) Phase field ϕ.

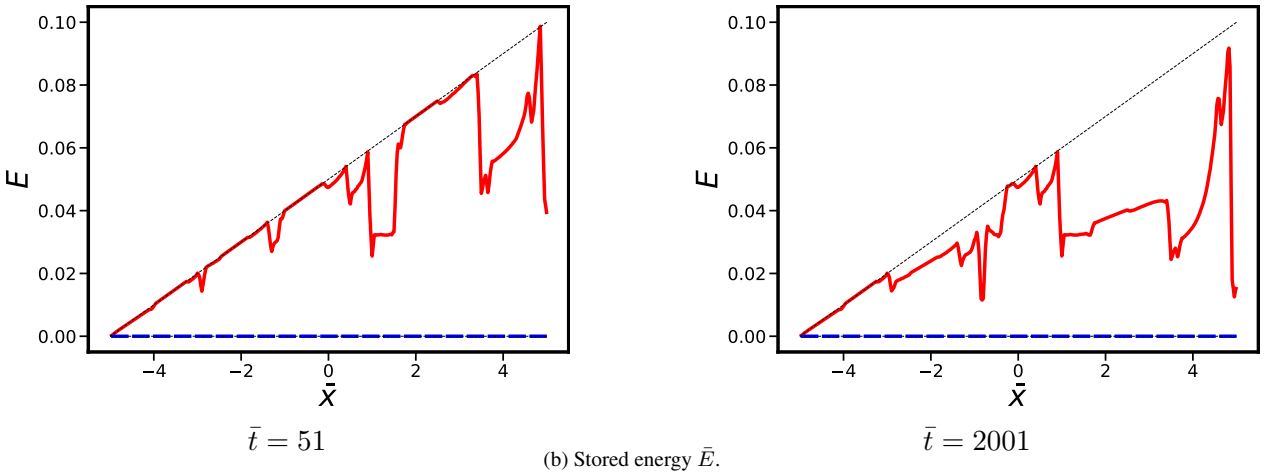

(b) Stored energy $\bar{E}$.

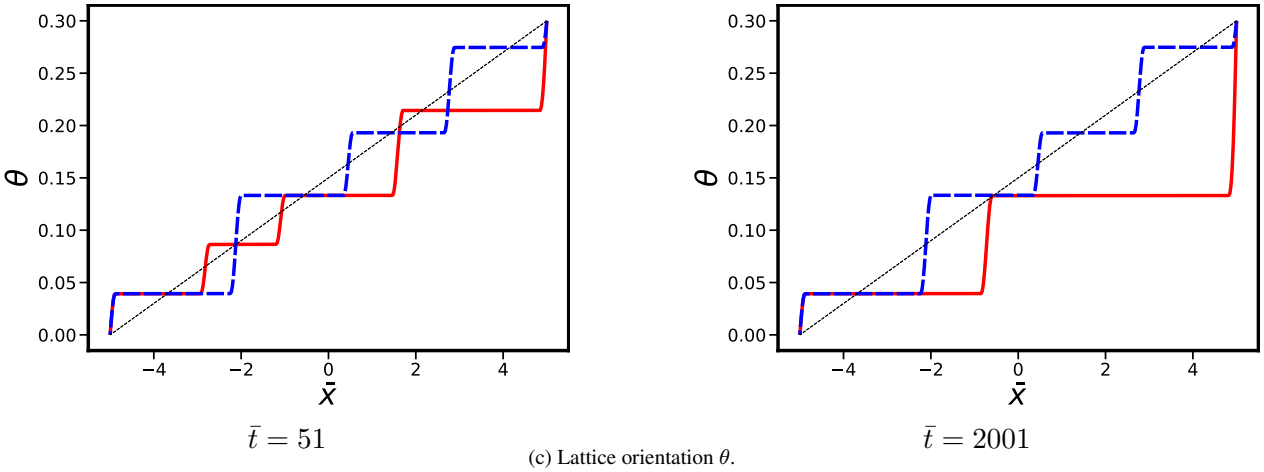

(c) Lattice orientation θ.

Fig. 16. Profiles of ϕ (top), $\bar{E}$ (middle) and θ (bottom) for a single crystal starting from uniform initial gradients of stored energy and orientation. The simulations are performed with the KWC model and are plotted at $\bar{t} = 51$ on the left and $\bar{t} = 2001$ on the right.

6. Grain nucleation during torsion of a single crystal rod

The KWC-Cosserat approach to grain nucleation and GB migration is now applied to a 3D structural problem for which orientation and SSD density gradients will be naturally induced by crystal plasticity in an initially homogeneous single crystal. The torsion of a cylindrical bar with circular cross-section made of a copper single crystal is computed by the finite element method. A 3D simulation framework is required by the anisotropy of the problem. Longitudinal rotation gradients are induced by torsion. Strain gradients are expected from the center to the outer surface of the bar. In addition, the cubic symmetry of the FCC crystal leads to gradients of plastic slip along the circumference of each cross-section as demonstrated numerically and experimentally by Nouailhas and Cailletaud (1995). This is due to the varying resolved shear stress on each slip system along the circumference. Torsion of elastic-plastic Cosserat bars was recently considered in the isotropic case by Ghiglione and Forest (2022), in the case of strain gradient crystal plasticity by Scherer et al. (2020) and Phalke et al. (2021) where various crystal orientation effects on crystal hardening were investigated. Torsion of a single crystal bar with square cross-section was performed using Cosserat crystal plasticity at finite strains by Blesgen (2015). The present simulations of KWC-Cosserat single crystal bars are the first of this kind. They are performed to show whether the gradients produced by torsion in a single crystal are sufficient to trigger GB formation and grain nucleation.

6.1. Problem setting

As shown in the above sections, the ability of the KWC model to handle grain nucleation in the presence of orientation gradients is naturally inherited in the coupled model. So far, these gradients were prescribed as initial conditions. In contrast, in this section the orientation gradients are produced through mechanical loading. Indeed we will show through numerical examples that the torsion of a single crystal rod with circular cross-section leads to a uniform orientation gradient along the axis of the cylinder. The computation is made of two loading sequences: first, a torsional loading is applied in order to generate plastic deformation and orientation gradients, then the deformation is held constant to let the microstructure evolve and simulate in that way annealing of the bar. The structure considered here is a cylinder with circular cross-section of radius $\bar{R} = 1$ and length $\bar{L} = 20$. Torsion is applied about the $[111]$ direction coinciding with the cylinder axis z. Under these conditions, only the 3 slip systems in the plane (111) are active: $[10\bar{1}](111)$, $[1\bar{1}0](111)$, $[01\bar{1}](111)$. All slip systems have an initial SSD density of $\bar{\rho}_0 = \rho_0/\Lambda = 0.1$. This initial dislocation density sets the initial critical resolved shear stress since the friction stress $\bar{\tau}_0$ was fixed to zero. The mesh is made of $25\,920$ hexahedral elements with quadratic shape functions, i.e. 20 node-bricks. Full integration is used with 27 Gauss points in each element, resulting in $109\,169$ nodes and $699\,840$ Gauss points. Since each node is endowed with 7 degrees of freedom, namely displacements $\bar{u}_x, \bar{u}_y, \bar{u}_z$, microrotation $\theta_x, \theta_y, \theta_z$ and order parameter ϕ, the size of the problem to be solved at each time step is $764\,183$ DOFs. The computation took 53 days on 24 Intel Xeon CPUs, requiring 112 GB of memory. The long computation time associated with very small time steps required by the strongly nonlinear KWC-Cosserat model explains while recent attempts have been made to implement more efficient solvers by Blesgen (2015); He and Admal (2021b). The initial conditions are uniform $\phi = 1$ and $\underline{\boldsymbol{\theta}} = \underline{\mathbf{0}}$. Dirichlet boundary conditions are imposed on $\bar{u}_x$, $\bar{u}_y$, $\bar{u}_z$ corresponding to a rigid rotation of the top/bottom surfaces of $\pm\vartheta$ around the z axis. Dirichlet boundary conditions $\theta_z = \pm\vartheta$ are also imposed on the top/bottom surfaces. Neumann conditions $m_{xz} = m_{yz} = 0$ are applied at the top/bottom as well. On the whole surface Neumann conditions are imposed for the order parameter ϕ such that $\underline{\boldsymbol{\xi}}_{\phi} \cdot \underline{\boldsymbol{n}} = 0$, where $\underline{\boldsymbol{n}}$ is the exterior normal. Finally, the lateral surfaces of the cylinder are free of all mechanical forces (zero traction and surface couples). After torsional loading at the prescribed angle ϑ the deformation is maintained according to table 3 to simulate annealing. The simulation was performed with the KWC-Cosserat model with Maxwell relaxation law in the GB region and parameters are given in table 4. They correspond to pure copper at about $200°C$ where only

self hardening is enabled ($h_{ij} = \delta_{ij}$). However, isotropic elasticity ($E = 130\ GPa,\ \nu = 0.3$) was adopted for simplicity. For more details about the choice of parameters, see Appendix A.

$\bar{t}$	0	1	730
Prescribed rotation ϑ	0	15°	15°

Tab. 3. Loading table for torsional loading

Parameter	$\bar{E}^e$	ν	$\bar{K}$	n	K_r	$\bar{d}$	χ	$\bar{\tau}_0$	$\bar{b}$	$\bar{\mu}$	h_1	h_2	h_3
Value	56 000	0.3	4.35	10	10	1×10^{-3}	0.3	0	0.2556×10^{-3}	21 750	1	0	0

Parameter	$\bar{\alpha}$	$\bar{s}$	$\bar{\varepsilon}$	$\bar{\eta}_\phi$	$\bar{\eta}^\star$	$\bar{\mu}_p$	β_p	C_D	$\bar{C}_A$	$\bar{\gamma}$	γ_g
Value	0.31	0.75	1	10	0.1	10^6	10^2	100	1	10^4	10^{-4}

Tab. 4. Model parameters used in the simulation of a single crystal bar under torsional loading.

6.2. Results

After deformation, tangential, radial and longitudinal rotation gradients are generated as shown in Fig. 17. In this figure the curvature tensor is computed in cylindrical coordinates and magnitude of the radial, tangential and longitudinal components are given by $|\bar{\underset{\sim}{\boldsymbol{\kappa}}} \cdot \underline{\boldsymbol{e}}_r|$, $|\bar{\underset{\sim}{\boldsymbol{\kappa}}} \cdot \underline{\boldsymbol{e}}_\theta|$ and $|\bar{\underset{\sim}{\boldsymbol{\kappa}}} \cdot \underline{\boldsymbol{e}}_z|$ respectively. The six-fold symmetry of the curvature and plastic deformation patterns is due to crystal symmetry of the (111) slip plane and associated slip systems. The gradient along the vertical direction z is two orders of magnitude larger than the gradients in the other directions. It is fairly uniform except close to the ends of the bar and is reminiscent of the initial conditions given in section 4.3. The cumulative plastic slip $\gamma^{tot} = \sum_{\alpha=1}^{3} |\gamma^\alpha|$ is shown in the cross-section of the middle of the rod in Fig. 17a. It can be seen that the cumulative plastic slip is made of concentric hexagons whose magnitude increases linearly from the center to the outer region of the cross-section up to about 3%. As illustrated in Fig. 18, the stored energy field generated by the loading is heterogeneous in the cross-section but its magnitude is rather low ($\max(\bar{E}) \sim 10^{-2}$), partly due to the fact that only self hardening was considered ($h_{ij} = \delta_{ij}$). Thus, according to equation (56), one expects local variations of ϕ of about 0.01 in the cross-section, which explains why the phase field is mostly impacted by the longitudinal torsion. After subsequent annealing, grain nucleation is observed in Fig. 19 in the form of a stack of pancake grains. As in section 5.3 grain nucleation is triggered by the rotation gradient. The SSD-based stored energy being low, the grains are rather homogeneous in the cross-section. We expect that increasing the magnitude of the torsion angle should still result in grains stacking along the rod, but the phase field should consist of concentric hexagons whose magnitude decreases linearly along the radius. The nucleation process being triggered by rotation gradients, it is not expected that grains will nucleate along the radius of the rod. Such a nucleation process would require the presence of multiple grains in the cross-section, or an additional mechanical loading prompting rotation gradients around the x or y axis. Another requirement would be to increase the radius of the rod, as the interface width ℓ_ϕ is larger than the radius ($\ell_\phi/R \sim 1.6$ in this computation). The profiles of ϕ and θ_z along the axis of the cylinder are shown in Fig. 20 and are very similar to those in section 4.3. The nucleation process in this figure is still quite in its early stage with misorientations ranging between $1^\circ - 3^\circ$. The model being computationally expensive, a later simulation stage is not available at the time and a rather coarse mesh has been used. However, we think that using a finer mesh will give quite similar qualitative results compared with the current mesh. In addition, it is expected that upon further annealing the different grains will merge along the vertical axis to accommodate the interface width ℓ_ϕ with misorientation between grains increasing up to forming a bicrystal for $\bar{t} \to \infty$,

as with the KWC model. Given the boundary conditions of the simulation, the bicrystal should have a final misorientation of about 30°.

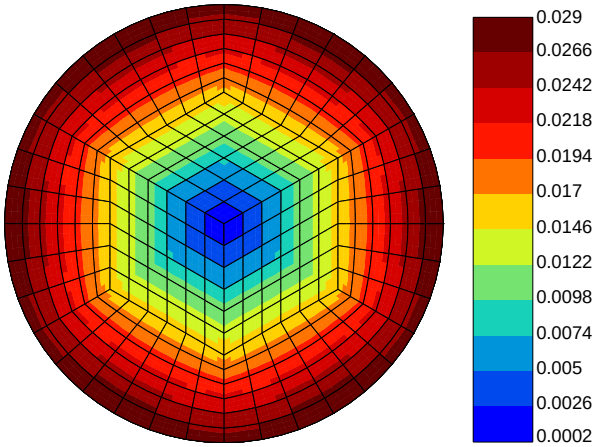

(a) Cumulative plastic slip on all 3 slip systems.

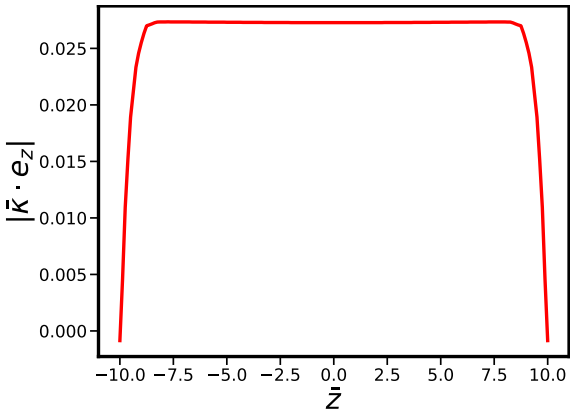

(b) Magnitude of the longitudinal curvature $|\bar{\underset{\sim}{\kappa}} \cdot \underline{e}_z|$ along the vertical direction.

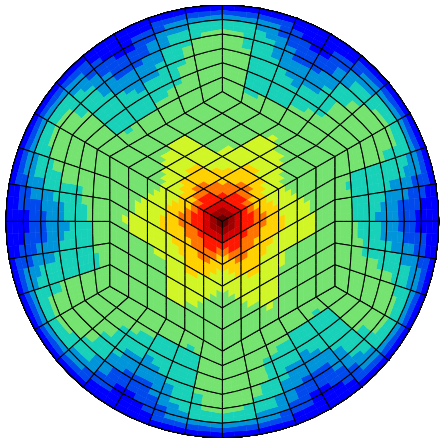

(c) Magnitude of the radial curvature $|\bar{\underset{\sim}{\kappa}} \cdot \underline{e}_r|$ in the middle cross-section.

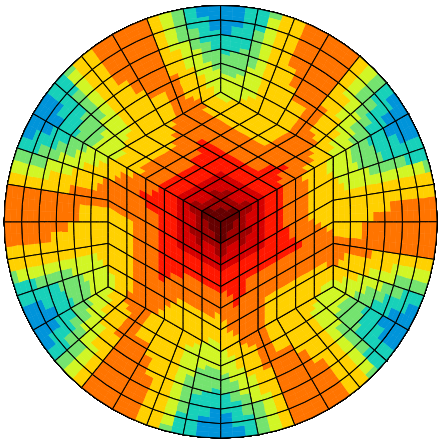

(d) Magnitude of the tangential curvature $|\bar{\underset{\sim}{\kappa}} \cdot \underline{e}_\theta|$ in the middle cross-section.

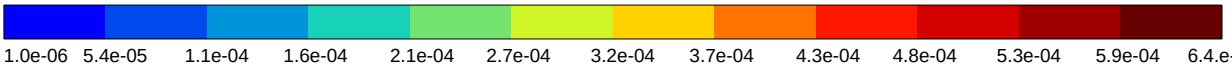

Fig. 17. Cumulative plastic slip in the middle cross-section (a); magnitudes of the curvatures in cylindrical coordinates in the longitudinal (b), radial (c) left) and tangential (d) directions after torsional loading of a single crystal rod.

In order to obtain nucleated grains with higher misorientation than in Fig. 20a, a similar computation was performed on a shorter rod of total length $\bar{L} = 10$ and the magnitude of the applied rotation was $\vartheta = 7.5°$. The mesh is made of 12960 hexahedral elements (20-node bricks), for a total of 55089 nodes, here with reduced integration, 8 Gauss points per element, to limit the computation time. The computation took approximately 178 days on 24 CPUs and required 50GB of memory. As visible in Fig. 21 and 22, grain nucleation is observed again after relaxation/annealing. The microstructure at the latest available time exhibits only three well-defined grains. Further microstructural evolution is still expected at a later stage.

6.3. Qualitative Comparison with experimental results from the literature

The simulations suggest that single crystal copper bars under torsion at sufficiently high temperature will recrystallize and a bamboo grain microstructure is expected to form. Torsion tests at high temperature are routinely performed for polycrystalline metals and alloys (Montheillet et al., 1984). They show typical

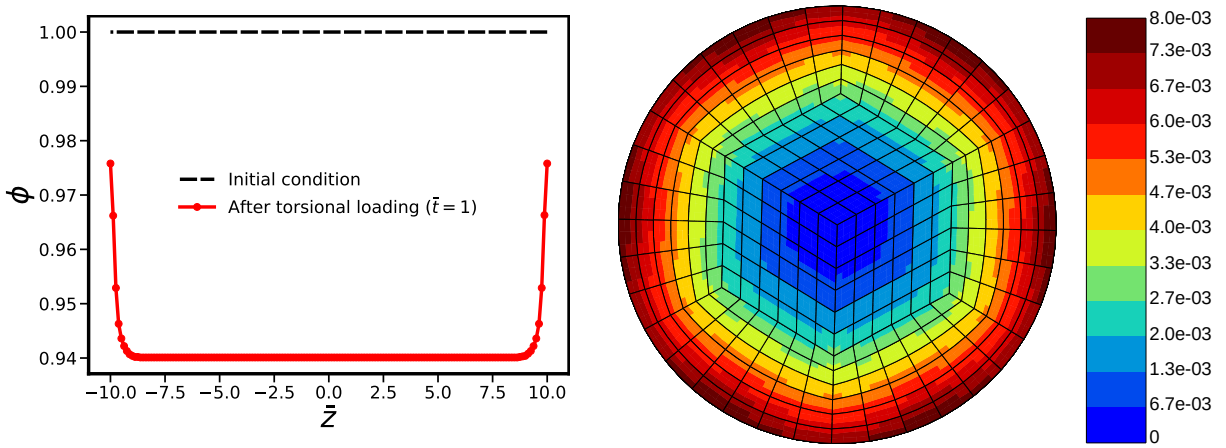

(a) Profile of ϕ along the vertical axis of the rod.

(b) Stored energy in the middle cross-section.

Fig. 18. Phase field ϕ (left) and stored energy $\bar{E}$ (right) after torsional loading of a single crystal rod.

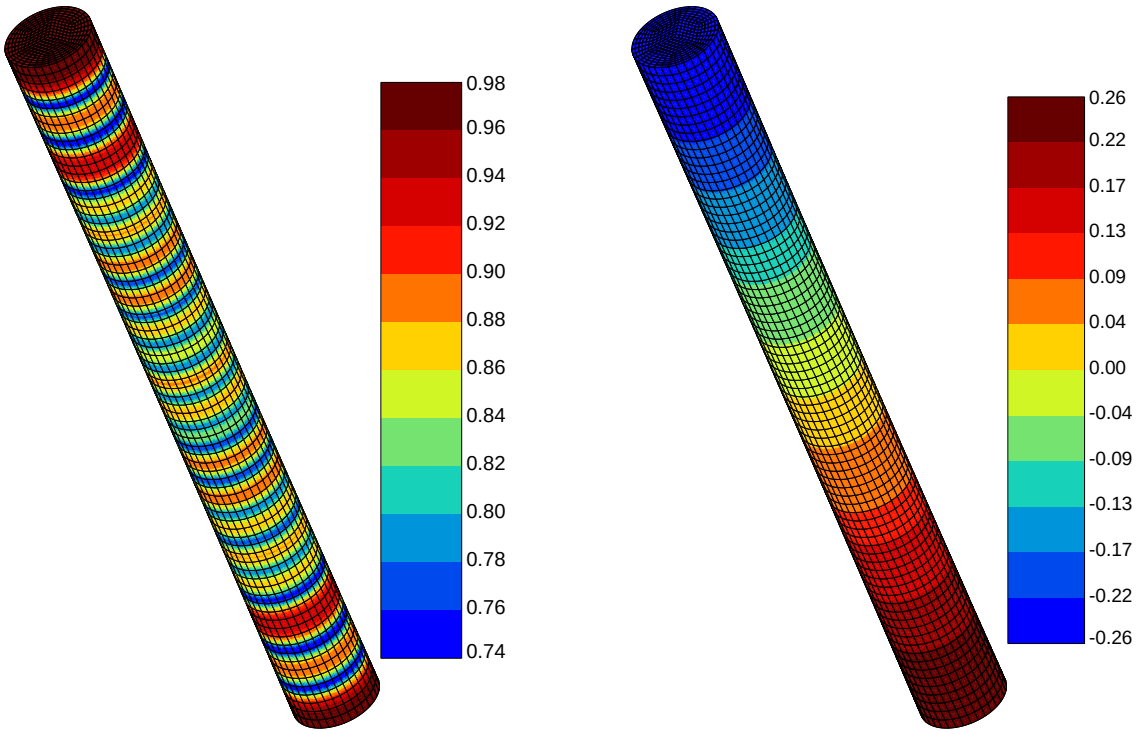

(a) Crystal order ϕ.

(b) Microrotation about $\underline{e}_z$.

Fig. 19. Phase field ϕ (left) and microrotation about $\underline{e}_z$ (right) after torsional loading and subsequent annealing of a single crystal rod.

oscillatory torque/angle responses due to successive recrystallization processes and strong crystallographic texture and grain morphology evolution. However, only a few papers deal with torsion of single crystal wires at high temperature. High pressure torsion of HCP Magnesium single crystals lead to recrystallization as shown in (Bonarski et al., 2008) but the observed grain morphology was unfortunately not described. Compression of aluminum single crystals and torsion of aluminum polycrystals also lead to recrystallization phenomena observed by Gourdet and Montheillet (2000). Kassner (1989) performed large strain torsion experiments on Al single crystals with the torsion axis parallel to [111], exactly the physical situation inves-

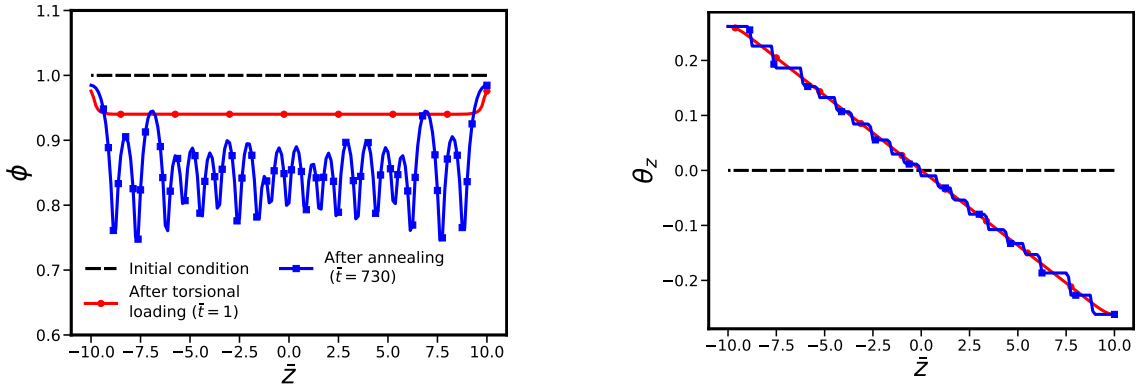

Fig. 20. Profiles of ϕ (left) and θ_z (right) along the axis of the cylinder after torsional loading and subsequent annealing ($\bar{t} = 730$).

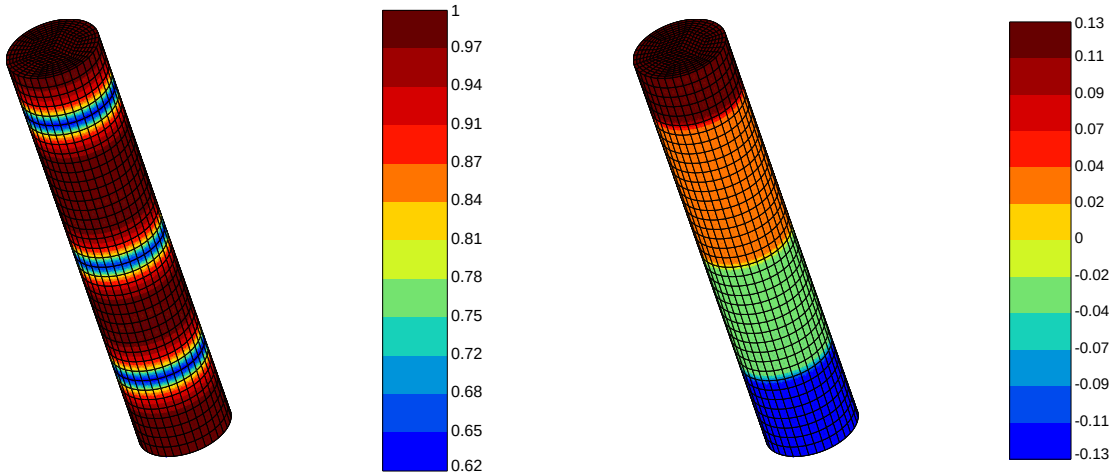

Fig. 21. Phase field ϕ (left) and microrotation about $\underline{\boldsymbol{e}}_z$ (right) after torsional loading and subsequent relaxation of a short single crystal rod ($\bar{t} = 5711$).

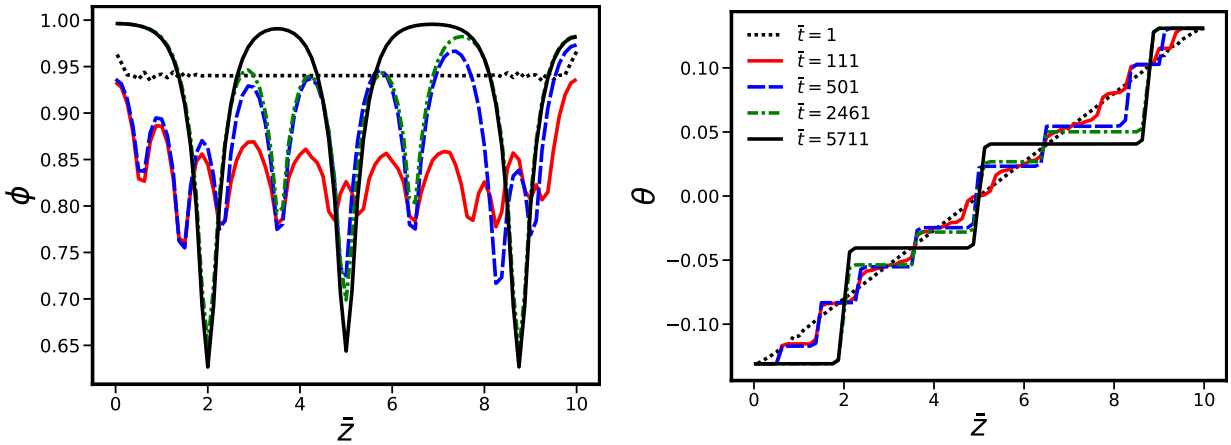

Fig. 22. Profiles of ϕ (left) and θ_z (right) along the axis of the cylinder after torsional loading and subsequent relaxation of the short single crystal of Fig. 21.

tigated in our simulations. This led to the early formation of geometrically necessary boundaries (GNBs) parallel to the slip plane and perpendicular to the torsion axis, in agreement with the present simulation re-

sults. The bamboo structure in the twisted rod can be observed in Fig. 3 of the paper by Kassner (1989) and is comparable to the simulation results of Fig. 19a. Despite the very large strains of about 16 under creep loading, only about 10% of the subgrain facets were found to be high angle boundaries (HABs) (Kassner and Barrabes, 2005). In that case the overall torque/angle curve did not display peak stress oscillations. The experimental results of Kassner (1989) therefore bring some experimental validation of the predicted microstructure evolution. However, the building-up of a low angle boundary bamboo grain structure predicted by the present simulations during torsion calls for more systematic and quantitative experimental validation.

7. Conclusions

A numerical stability analysis of orientation gradients and gradients of stored energy was performed for the KWC and KWC-Cosserat phase field models.

The ability of the KWC model to simulate grain nucleation in a single crystal in the presence of orientation gradients without the need to introduce seeds was demonstrated through 1D numerical examples. According to the simulations, the initial single crystal is fragmented into a multitude of grains with low misorientation (LAB) that grow and merge due to the interaction between diffuse grain boundary zones. By tracking the time evolution of the total energy, it was shown that grain nucleation contributes to the minimization of total energy. It was demonstrated that the presence of orientation gradients is necessary to trigger grain nucleation, as a gradient of stored energy in a single crystal cannot lead by itself to the formation of new grains, according to the model. Gradients of stored energy influence the mobility of newly formed grain and subgrain boundaries.

A similar study was carried out with the KWC-Cosserat model of Ask et al. (2020) to investigate mechanical effects on grain nucleation, firstly in the absence of overall loading. Special attention was drawn on the development and relaxation of skew-symmetric stresses during the formation and the migration of grain boundaries. Two different types of evolution law of the reference orientation – required to relax skew-symmetric stresses at the grain boundaries – were considered: a Maxwell viscoelastic model and a Norton viscoplastic model with threshold. It was shown that the stress profiles along the bicrystal share similarities with the elasto-plastic theory of dislocations and disclinations (Taupin et al., 2013). The introduction of a threshold in the relaxation law leads to residual stresses that delay grain boundary motion and nucleation. Sufficiently high values of the threshold can impede grain nucleation within an orientation gradient.

A 3D finite element simulation combining crystal plasticity and grain boundary formation was then performed for the torsion of a single crystal bar with circular cross-section. Initial quasi-static torsion was followed by simulation of the annealing process during a relaxation stage. The torsion axis was aligned with the [111] direction of the FCC crystal. The torsional loading generated a significant rotation gradient along the cylinder axis that was sufficient to trigger grain nucleation in the form of a stack of cylindrical grains with low angle grain boundaries, in agreement with the 1D stability analysis. The radial and circumferential gradients of SSD-based stored energy induced by heterogeneous plastic slip in the cross-sections are too low in magnitude to trigger subgrain formation in the cross-section. This results in a bamboo-like subgrain microstructure in the wire. Experimental support of the torsion simulation result was found in the case of torsion of aluminum single crystals under creep loading in (Kassner, 1989; Kassner and Barrabes, 2005) where stacks of LABs were observed parallel to the (111) planes.

The results of the present work open new perspectives in the full field simulation of microstructure evolution in plastically deformed crystals, including thermomechanical treatments of metals and alloys. It is remarkable that the KWC-Cosserat model predicts the formation of subgrain boundaries in single crystals due to the development of orientation gradients. The proposed analysis remains rather qualitative and significant additional effort is needed to address specific materials with proper parameter identification over a given temperature range. This includes consideration of anisotropic GB energy as done by Admal et al. (2019) for the KWC model. The KWC-Cosserat model and suitable extensions for specific recrystallization

mechanisms are promising tools for the simulation of recrystallization phenomena without *ad hoc* introduction of random seeds in crystal plasticity phase field simulations. Stochastic aspects of grain nucleation will emerge from the strongly heterogeneous nature of plastic deformation in single and polycrystals.

KWC-Cosserat modeling entails considerable computational challenges due to the stiff nonlinearity of the model and the large number of unknowns including degrees of freedom and internal variables. In view of the model complexity, alternative more sophisticated algorithms and model simplifications are proposed by Kim et al. (2021); He and Admal (2021b) and Baek et al. (2022) for more efficient computing and accuracy.

Acknowledgements

The authors are grateful to the CNRS for the funding of this research through the 80Prime 2020 COSX interdisciplinary project.

Appendix A. Identification of parameters

We recall that the dimensionless KWC free energy is of the following form

$$\bar{\psi}(\bar{\nabla}\theta, \phi, \bar{\nabla}\phi) = \psi(\nabla\theta, \phi, \nabla\phi)/f_0 = f(\phi) + \frac{\bar{\alpha}^2}{2}\left|\bar{\nabla}\phi\right|^2 + \bar{s}g(\phi)\left|\bar{\nabla}\theta\right| + \frac{\bar{\varepsilon}^2}{2}h(\phi)\left|\bar{\nabla}\theta\right|^2$$

The phase field parameters $\bar{\alpha}$ and $\bar{s}$ in the free enery density can be calibrated using the asymptotic analysis of Lobkovsky and Warren (2001) to fit a grain boundary energy misorientation curve found in the literature (see Figure 1 in Ask et al. (2020)). The misorientation is capped at $\Delta\theta = 30^\circ$ to include only the Read-Shockley part of the curve and discard the local GB energy cusps. A grain boundary energy magnification factor f_a can be defined such that

$$f_a = \frac{\gamma_{ref}(\Delta\theta = 30^\circ)}{\widetilde{\gamma}(\Delta\theta = 30^\circ)} = f_0\Lambda\bar{\varepsilon}, \quad \gamma(\Delta\theta) = \widetilde{\gamma}(\Delta\theta) \times f_a \tag{A.1}$$

where $\gamma_{ref}(\Delta\theta = 30^\circ)$ and $\widetilde{\gamma}(\Delta\theta = 30^\circ)$ are the reference (used to calibrate the parameters) and asymptotic grain boundary energies, respectively, for a misorientation of 30°. The parameter $\bar{\varepsilon}$ in the free energy density, which controls the grain boundary diffusivity, can be chosen freely. The parameters are calibrated for pure copper with $g(\phi) = -2\left(\log(1-\phi) + \phi\right)$. At the mesoscale, appropriate length scale Λ and time scale τ_0 are respectively $\Lambda = 1\,\mu\mathrm{m}$ and $\tau_0 = 1\,\mathrm{s}$. This calibration method gives $\bar{s} = 0.75$ and $\bar{\alpha} = 0.31$ for $\bar{\varepsilon} = 1$. The grain boundary energy is fitted against that of a $\langle 100\rangle$ Cu tilt boundary obtained from atomistic simulations (Wolf, 1990), see Fig. A.23a. The grain boundary energy scale factor is $f_a = 2300\,\mathrm{mJ\,m^{-2}}$, which corresponds to a grain boundary energy scale parameter $f_0 = \frac{f_a}{\Lambda\bar{\varepsilon}} = 2.3\,\mathrm{MPa}$.

As there is no published asymptotic analysis that accounts for grain boundary migration due to a stored energy difference, the mobility parameters $\bar{\eta}_\phi, \bar{\eta}_\theta, \bar{\mu}_p, \beta_p$ must be tuned so that the resulting mobility of a 1D boundary subjected to a stored energy difference is comparable to the data found in the literature (Gottstein and Shvindlerman, 2009). The recovery parameters $\bar{C}_A, C_D$ are chosen so that full recovery, i.e. annihilation of stored dislocations, occurs behind the moving grain boundary.

Data related to the grain boundary mobility of pure copper can be found in the work of Vandermeer et al. (1997), where mobilities for a wide range of temperatures are presented, which can be used as a reference to estimate the temperature in the KWC model. The data used in Fig. 5 of this reference is plotted in Fig. A.23b. The basic test of a bicrystal with a lattice misorientation of 0.3 subjected to a stored energy difference of 0.09 is carried out for the KWC and KWC-Cosserat models. In the simulations with both models the initial state is in equilibrium. To do this, a KWC simulation is run to find the fields ϕ, θ at equilibrium, followed by a KWC-Cosserat calculation to start from a stress-free state. The results are given in table A.5.

For the KWC-Cosserat model, the parameters related to the mechanical behavior are adapted from the literature for pure copper, e.g. Gérard et al. (2009) and Cheong and Busso (2004). The different parameters involved and their dimensionless versions are summarized in table A.6.

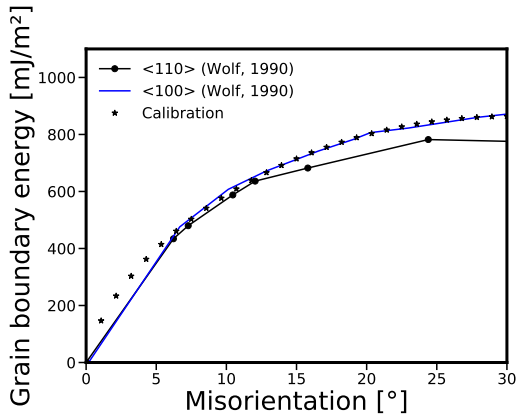

(a) Calibration of the grain boundary energy–misorientation curve.

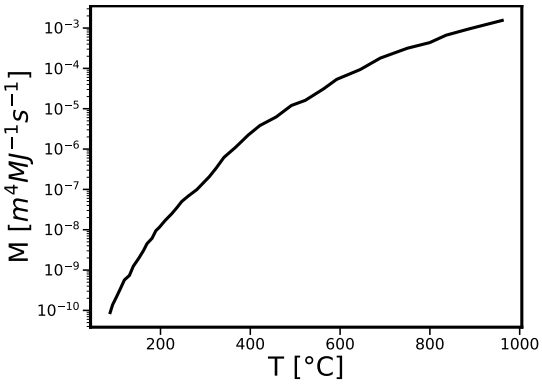

(b) Pure copper grain boundary mobility as a function of temperature, adapted from Vandermeer et al. (1997).

Fig. A.23. Grain boundary energy–misorientation curve (left) and grain boundary–temperature curve (right) used for the identification of parameters for copper.

Model	$\bar{\eta}_\theta$ or $\bar{\eta}^\star$	β_p	GB mobility$\times 10^{-8}\mathrm{m}^4/\mathrm{MJ/s}$	Temperature °C
KWC	0.1	100	2.4	~ 225
	1	1000	2.2	~ 220
KWC-Cosserat	0.1	100	1.5	~ 205
	1.	1000	1.5	~ 205

Tab. A.5. Stored energy driven migration in a bicrystal for different mobility parameters. Parameters $\bar{\mu}_p = 10^6, \bar{\eta}_\phi = 10$ are fixed.

Appendix B. Matched asymptotics analysis

The profiles of ϕ and θ as well as the grain boundary energy and mobility predicted by the KWC model can be obtained by a formal asymptotic expansion as shown by Lobkovsky and Warren (2001). The main idea is based on the definition of the grain boundary as the strip S between two non-intersecting smooth curves Γ^- and Γ^+ where $\nabla\theta \neq 0$. An explicit, semi-analytical solution can be found for a flat, stationary interface described in Fig. B.24. A stretched coordinate $z = \frac{r}{\bar{\varepsilon}}$ is introduced and three regions can be identified:

- Far from the interface, i.e. $|z| \to \infty$, the fields are constant such that $\nabla\phi = 0$ and $\nabla\theta = 0$.
- In an intermediate region for $|z| > \delta z$, only θ is constant such that $\nabla\theta = 0$ but $\nabla\phi \neq 0$.
- Finally, in an inner region where $z < \delta z$ both gradients are non zero, i.e. $\nabla\phi \neq 0, \quad \nabla\theta \neq 0$.

The fields are expanded into power series of $\bar{\varepsilon}$:

$$\begin{cases} \phi = \phi^0 + \bar{\varepsilon}\phi^1 + ... \\ \theta = \theta^0 + \bar{\varepsilon}\theta^1 + ... \end{cases}$$

and the parameters $\bar{\alpha}$ and $\bar{s}$ are scaled with respect to $\bar{\varepsilon}$ as follows:

$$\widetilde{\alpha} = \bar{\alpha}/\bar{\varepsilon},\ \widetilde{s} = \bar{s}/\bar{\varepsilon},\ \widetilde{\eta}_\phi = \bar{\eta}_\phi/\bar{\varepsilon}^2,\ \widetilde{\eta}_\theta = \bar{\eta}_\theta/\bar{\varepsilon}^2$$

so as to ensure that the intermediate and inner regions scale like $\mathcal{O}(\bar{\epsilon})$ as $\bar{\epsilon} \to 0$, and that a flat interface does not move (Lobkovsky and Warren, 2001).

Parameter/ property	Unit	Dimensionless expression	Comment
τ_0	s	-	Time scale
Λ	µm	-	Length scale
f_0	$\mathrm{J\,m^{-3}}$	-	Energy scale
α	m	$\bar{\alpha} = \alpha/\Lambda$	Phase field parameters
s	m	$\bar{s} = s/\Lambda$	
ε	m	$\bar{\varepsilon} = \varepsilon/\Lambda$	
η_ϕ	$\mathrm{J\,s\,m^{-3}}$	$\bar{\eta}_\phi = \eta_\phi/(f_0\tau_0)$	Mobility for ϕ
$\eta^\star$	$\mathrm{J\,s\,m^{-3}}$	$\bar{\eta}^\star = \eta^\star/(f_0\tau_0)$	Mobility for $\underline{\boldsymbol{\theta}}^\star$
μ_p	m	$\bar{\mu}_p = \mu_p/\Lambda$	Parameters for the localization function $P(\nabla\theta)$
β_p	-	-	
E^e	MPa	$\bar{E}^e = E/f_0$	Young's modulus
ν	-	-	Poisson's ratio
K	$\mathrm{MPa\,s^{1/n}}$	$\bar{K} = K/f_0$	Viscoplasticity parameters
n	-	-	
τ_c	MPa	$\bar{\tau}_c = \tau_c/f_0$	Critical resolved shear stress
χ	-	-	Coefficient
μ	MPa	$\bar{\mu} = \mu/f_0$	Mean shear modulus
K_r	-	-	Kocks-Mecking parameters
d	m	$\bar{d}_r = d_r/\Lambda$	
b	m	$\bar{b} = b/\Lambda$	Burgers vector
C_A	$\mathrm{m^2}$	$\bar{C}_A = C_A/\Lambda^2$	Parameters for recovery
C_D	-	-	
γ	m	$\bar{\gamma} = \gamma/\Lambda$	Regularization for $\lvert\bar{\nabla}\theta\rvert$
γ_g	-	-	Regularization for $g(\phi) = -2(\log(1-\phi)+\phi)$

Tab. A.6. Parameters in the KWC-Cosserat model.

Inserting the expansions and scalings into the PDEs give series of PDEs for the functions at the different orders (e.g. ϕ^0 and θ^0, ϕ^1 and θ^1 etc). The problem is then solved order by order, using matching conditions between the different regions. The interface width and energy as well as the stationary profiles are obtained using the 0^{th} order solution whereas the interface mobility and velocity are obtained using the 1^{st} order solution. Note that this analysis has not been extended to account for stored energy driven migration. The profiles of ϕ^0 and θ^0 are obtained by integrating

$$\frac{\partial\phi^0}{\partial z} = \begin{cases} \frac{1}{\tilde{\alpha}}\sqrt{2f^0 - \frac{\tilde{s}^2}{h^0}\left(g^0(\phi^0_{max}) - g^0\right)}, & \phi^0_{min} \le \phi^0 \le \phi^0_{max} \\ \frac{1}{\tilde{\alpha}}\sqrt{2f^0}, & \phi^0_{max} < \phi^0 \le 1 \end{cases} \tag{B.1}$$

$$\frac{\partial\theta_0}{\partial z} = \tilde{s}\frac{g^0(\phi^0_{max}) - g(\phi^0)}{h^0(\phi^0)}, \quad 0 \le z \le \delta z \tag{B.2}$$

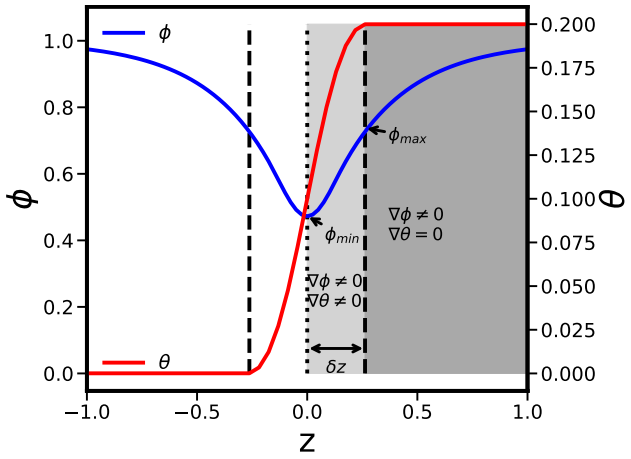

Fig. B.24. Schematic representation of the solution for a flat static interface between two grains.

The values of ϕ^0_{min} (at $z = 0$) and ϕ^0_{max} (at the junction δz between the inner and intermediate regions) are obtained from

$$\frac{\widetilde{s}}{2}\frac{\left(g^0(\phi^0_{max}) - g^0(\phi^0_{min})\right)^2}{h^0(\phi^0_{min})} - f^0(\phi^0_{min}) = 0 \tag{B.3}$$

$$\frac{\Delta\theta}{2} = \int_{\phi^0_{min}}^{\phi^0_{max}} \frac{\partial\theta^0}{\partial z}\frac{\partial z}{\partial\phi^0}d\phi^0 \tag{B.4}$$

The half interface width $\ell_\theta/2$ is given by

$$\ell_\theta/2 = \delta z = \widetilde{\alpha}\int_{\phi^0_{min}}^{\phi^0_{max}} \frac{1}{2f^0 - \frac{\widetilde{s}^2}{h^0}\left(g^0(\phi^0_{max}) - g^0\right)}d\phi^0 \tag{B.5}$$

Finally, the grain boundary energy is found as

$$2\widetilde{\alpha}^2\int_{\phi^0_{min}}^{1}\frac{\partial\phi^0}{\partial z}d\phi^0 + \widetilde{s}g^0(\phi^0_{max})\Delta\theta \tag{B.6}$$

Appendix C. Three-dimensional finite element implementation of the KWC-Cosserat model

Although formulated in a three-dimensional framework in Ask et al. (2018b, 2020), the KWC-Cosserat model has so far only been implemented in a two-dimensional finite element formulation. In this section, details of its implementation in 3D are given since it is required for the simulation of the torsion of a single crystal rod presented in this work. The framework is still that of small deformation, rotation and curvature with grain boundary energy independent of the boundary plane. The weak form of the balance equations (35)–(37) is obtained after multiplication by a virtual field, integration over the whole domain and use of the divergence theorem, such that

$$-\int_V \left(\underset{\sim}{\boldsymbol{\sigma}}^s : \underline{\boldsymbol{u}} \otimes \nabla^s + \underline{\boldsymbol{\pi}}_\theta \cdot \overset{\times}{\underline{\omega}}\right) dV + \int_{\partial V} \underline{\boldsymbol{u}} \cdot \underline{\boldsymbol{t}}\, dS = 0 \tag{C.1}$$

$$\int_V \left(-\underset{\sim}{\boldsymbol{\xi}}_\theta : \underline{\boldsymbol{\theta}} \otimes \nabla + \underline{\boldsymbol{\theta}} \cdot \underline{\boldsymbol{\pi}}_\theta\right) dV + \int_{\partial V} \underline{\boldsymbol{\theta}} \cdot \underset{\sim}{\boldsymbol{\xi}}_\theta \cdot \underline{\boldsymbol{n}}\, dS = 0 \tag{C.2}$$

$$\int_V \left(-\underline{\boldsymbol{\xi}}_\phi \cdot \nabla\phi + \phi \cdot \pi_\phi\right) dV + \int_{\partial V} \phi \cdot \underline{\boldsymbol{\xi}}_\phi \cdot \underline{\boldsymbol{n}}\, dS = 0 \tag{C.3}$$

with $\underline{\boldsymbol{\pi}}_\theta = 2\,\overset{\times}{\underline{\sigma}}$, $\underline{\boldsymbol{t}} = \underset{\sim}{\boldsymbol{\sigma}} \cdot \underline{\boldsymbol{n}}$, $\underline{\boldsymbol{M}} = \underset{\sim}{\boldsymbol{\xi}}_\theta \cdot \underline{\boldsymbol{n}}$. The displacement, Cosserat microrotation and phase fields are interpolated at the n nodes of each element such that

$$\underline{\boldsymbol{u}}\,(\underline{\boldsymbol{x}}\,,t) = \sum_{i=1}^{n} N_{ij}^{e^u}(\underline{\boldsymbol{x}}\,)\underline{\boldsymbol{u}}\,_j^e(t), \quad \underline{\boldsymbol{\theta}}\,(\underline{\boldsymbol{x}}\,,t) = \sum_{i=1}^{n} N_{ij}^{e^\theta}(\underline{\boldsymbol{x}}\,)\underline{\boldsymbol{\theta}}\,_j^e(t), \quad \underline{\boldsymbol{\phi}}\,(\underline{\boldsymbol{x}}\,,t) = \sum_{i=1}^{n} N_i^e(\underline{\boldsymbol{x}}\,)\underline{\boldsymbol{\phi}}\,_i^e(t) \tag{C.4}$$

with the nodal values arranged as follows:

$$\phi^e(t) = \begin{pmatrix} \phi^1 & \phi^2 & \phi^3 & \dots & \phi^n \end{pmatrix}^T \tag{C.5}$$

$$\underline{\boldsymbol{u}}\,^e(t) = \begin{pmatrix} u_1^1 & u_2^1 & u_3^1 & u_1^2 & u_2^2 & u_3^2 & \dots & u_1^n & u_2^n & u_3^n \end{pmatrix}^T \tag{C.6}$$

$$\underline{\boldsymbol{\theta}}\,^e(t) = \begin{pmatrix} \theta_1^1 & \theta_1^2 & \dots & \theta_1^n & \theta_2^1 & \theta_2^2 & \dots & \theta_2^n & \theta_3^1 & \theta_3^2 & \dots & \theta_3^n \end{pmatrix}^T \tag{C.7}$$

The shape functions are thus:

$$N_i^e = \begin{bmatrix} N_1 & N_2 & N_3 & \dots & N_n \end{bmatrix} \tag{C.8}$$

$$N_{ij}^{e^u} = \begin{bmatrix} N_1 & 0 & 0 & N_2 & 0 & 0 & \dots & N_n & 0 & 0 \\ 0 & N_1 & 0 & 0 & N_2 & 0 & \dots & 0 & N_n & 0 \\ 0 & 0 & N_1 & 0 & 0 & N_2 & \dots & 0 & 0 & N_n \end{bmatrix} \tag{C.9}$$

$$N_{ij}^{e^\theta} = \begin{bmatrix} N_1 & N_2 & \dots & N_n & 0 & 0 & \dots & 0 & 0 & 0 & \dots & 0 \\ 0 & 0 & \dots & 0 & N_1 & N_2 & \dots & N_n & 0 & 0 & \dots & 0 \\ 0 & 0 & \dots & 0 & 0 & 0 & \dots & 0 & N_1 & N_2 & \dots & N_n \end{bmatrix} \tag{C.10}$$

The discrete gradients of the degrees of freedom in the element are given by

$$\nabla\phi(\underline{\boldsymbol{x}}\,,t) = \sum_{i=1}^{n} B_{ij}^{e^\phi}\phi_j^e(t), \quad \underline{\boldsymbol{\theta}}\,(\underline{\boldsymbol{x}}\,,t) \otimes \nabla = \sum_{i=1}^{n} \underset{\sim}{\boldsymbol{B}}_{ij}^{e^\theta}(\underline{\boldsymbol{x}}\,)\underline{\boldsymbol{\theta}}\,_j^e(t) \tag{C.11}$$

$$\underline{\boldsymbol{u}}\,(\underline{\boldsymbol{x}}\,,t) \otimes \nabla^s = \sum_{i=1}^{n} \underset{\sim}{\boldsymbol{B}}_{s_{ij}}^{e^u}(\underline{\boldsymbol{x}}\,)\underline{\boldsymbol{u}}\,_j^e(t), \quad \overset{\times}{\underline{\omega}}\,(\underline{\boldsymbol{x}}\,,t) = \sum_{i=1}^{n} \underset{\sim}{\boldsymbol{B}}_{\omega_{ij}}^{e^u}(\underline{\boldsymbol{x}}\,)\underline{\boldsymbol{u}}\,_j^e(t) \tag{C.12}$$

such that

$$\begin{bmatrix} u_{1,1} \\ u_{2,2} \\ u_{3,3} \\ \sqrt{2}\varepsilon_{12} \\ \sqrt{2}\varepsilon_{23} \\ \sqrt{2}\varepsilon_{31} \end{bmatrix} = \underbrace{\begin{bmatrix} \frac{\partial N_1}{\partial x} & 0 & 0 & \frac{\partial N_2}{\partial x} & 0 & 0 & \dots & \frac{\partial N_n}{\partial x} & 0 & 0 \\ 0 & \frac{\partial N_1}{\partial y} & 0 & 0 & \frac{\partial N_2}{\partial y} & 0 & \dots & 0 & \frac{\partial N_n}{\partial y} & 0 \\ 0 & 0 & \frac{\partial N_1}{\partial z} & 0 & 0 & \frac{\partial N_2}{\partial z} & \dots & 0 & 0 & \frac{\partial N_1}{\partial z} \\ \frac{1}{\sqrt{2}}\frac{\partial N_1}{\partial y} & \frac{1}{\sqrt{2}}\frac{\partial N_1}{\partial x} & 0 & \frac{1}{\sqrt{2}}\frac{\partial N_2}{\partial y} & \frac{1}{\sqrt{2}}\frac{\partial N_2}{\partial x} & 0 & \dots & \frac{1}{\sqrt{2}}\frac{\partial N_n}{\partial y} & \frac{1}{\sqrt{2}}\frac{\partial N_n}{\partial x} & 0 \\ 0 & \frac{1}{\sqrt{2}}\frac{\partial N_1}{\partial z} & \frac{1}{\sqrt{2}}\frac{\partial N_1}{\partial y} & 0 & \frac{1}{\sqrt{2}}\frac{\partial N_2}{\partial z} & \frac{1}{\sqrt{2}}\frac{\partial N_2}{\partial y} & \dots & 0 & \frac{1}{\sqrt{2}}\frac{\partial N_n}{\partial z} & \frac{1}{\sqrt{2}}\frac{\partial N_n}{\partial y} \\ \frac{1}{\sqrt{2}}\frac{\partial N_1}{\partial z} & 0 & \frac{\partial N_1}{\partial x} & \frac{1}{\sqrt{2}}\frac{\partial N_2}{\partial z} & 0 & \frac{\partial N_2}{\partial x} & \dots & \frac{1}{\sqrt{2}}\frac{\partial N_n}{\partial z} & 0 & \frac{\partial N_1}{\partial x} \end{bmatrix}}_{[\underset{\sim}{\boldsymbol{B}}^{e^u}_s]} \cdot \begin{pmatrix} u_1^1 \\ u_2^1 \\ u_3^1 \\ u_1^2 \\ u_2^2 \\ u_3^2 \\ \vdots \\ u_1^n \\ u_2^n \\ u_3^n \end{pmatrix} \tag{C.13}$$

$$\begin{bmatrix}\omega_1\\ \omega_2\\ \omega_3\end{bmatrix} = \underbrace{\begin{bmatrix} 0 & -\frac{1}{2}\frac{\partial N_1}{\partial z} & \frac{1}{2}\frac{\partial N_1}{\partial y} & 0 & -\frac{1}{2}\frac{\partial N_2}{\partial z} & \frac{1}{2}\frac{\partial N_2}{\partial y} & \dots & 0 & -\frac{1}{2}\frac{\partial N_n}{\partial z} & \frac{1}{2}\frac{\partial N_n}{\partial y} \\ \frac{1}{2}\frac{\partial N_1}{\partial z} & 0 & -\frac{1}{2}\frac{\partial N_1}{\partial x} & \frac{1}{2}\frac{\partial N_2}{\partial z} & 0 & -\frac{1}{2}\frac{\partial N_2}{\partial x} & \dots & \frac{1}{2}\frac{\partial N_n}{\partial z} & 0 & -\frac{1}{2}\frac{\partial N_1 n}{\partial x} \\ -\frac{1}{2}\frac{\partial N_1}{\partial y} & \frac{1}{2}\frac{\partial N_1}{\partial x} & 0 & -\frac{1}{2}\frac{\partial N_2}{\partial y} & \frac{1}{2}\frac{\partial N_2}{\partial x} & 0 & \dots & -\frac{1}{2}\frac{\partial N_n}{\partial y} & \frac{1}{2}\frac{\partial N_n}{\partial x} & 0 \end{bmatrix}}_{[\underset{\sim}{\boldsymbol{B}}^{e^u}_{\omega}]} \cdot \begin{pmatrix} u_1^1 \\ u_2^1 \\ u_3^1 \\ u_1^2 \\ u_2^2 \\ u_3^2 \\ \vdots \\ u_1^n \\ u_2^n \\ u_3^n \end{pmatrix} \tag{C.14}$$

$$\begin{bmatrix}\theta_{1,1}\\ \theta_{2,2}\\ \theta_{3,3}\\ \theta_{1,2}\\ \theta_{2,3}\\ \theta_{3,1}\\ \theta_{2,1}\\ \theta_{3,2}\\ \theta_{1,3}\end{bmatrix} = \underbrace{\begin{bmatrix} \frac{\partial N_1}{\partial x} & \frac{\partial N_2}{\partial x} & \dots & \frac{\partial N_n}{\partial x} & 0 & 0 & \dots & 0 & 0 & 0 & \dots & 0 \\ 0 & 0 & \dots & 0 & \frac{\partial N_1}{\partial y} & \frac{\partial N_2}{\partial y} & \dots & \frac{\partial N_n}{\partial y} & 0 & 0 & \dots & 0 \\ 0 & 0 & \dots & 0 & 0 & 0 & \dots & 0 & \frac{\partial N_1}{\partial z} & \frac{\partial N_2}{\partial z} & \dots & \frac{\partial N_n}{\partial z} \\ \frac{\partial N_1}{\partial y} & \frac{\partial N_2}{\partial y} & \dots & \frac{\partial N_n}{\partial y} & 0 & 0 & \dots & 0 & 0 & 0 & \dots & 0 \\ 0 & 0 & \dots & 0 & \frac{\partial N_1}{\partial z} & \frac{\partial N_2}{\partial z} & \dots & \frac{\partial N_n}{\partial z} & 0 & 0 & \dots & 0 \\ 0 & 0 & \dots & 0 & 0 & 0 & \dots & 0 & \frac{\partial N_1}{\partial x} & \frac{\partial N_2}{\partial x} & \dots & \frac{\partial N_n}{\partial x} \\ 0 & 0 & \dots & 0 & \frac{\partial N_1}{\partial x} & \frac{\partial N_2}{\partial x} & \dots & \frac{\partial N_n}{\partial x} & 0 & 0 & \dots & 0 \\ 0 & 0 & \dots & 0 & 0 & 0 & \dots & 0 & \frac{\partial N_1}{\partial y} & \frac{\partial N_2}{\partial y} & \dots & \frac{\partial N_n}{\partial y} \\ \frac{\partial N_1}{\partial z} & \frac{\partial N_2}{\partial z} & \dots & \frac{\partial N_n}{\partial z} & 0 & 0 & \dots & 0 & 0 & 0 & \dots & 0 \end{bmatrix}}_{\left[\underset{\sim}{\boldsymbol{B}}^{e^\theta}\right]} \cdot \begin{pmatrix} \theta_1^1 \\ \theta_1^2 \\ \vdots \\ \theta_1^n \\ \theta_2^1 \\ \theta_2^2 \\ \vdots \\ \theta_2^n \\ \theta_3^1 \\ \theta_3^2 \\ \vdots \\ \theta_3^n \end{pmatrix} \tag{C.15}$$

$$\begin{pmatrix}\phi_{,1}\\ \phi_{,2}\\ \phi_{,3}\end{pmatrix} = \underbrace{\begin{bmatrix} \frac{\partial N_1}{\partial x} & \frac{\partial N_2}{\partial x} & \dots & \frac{\partial N_1}{\partial n} \\ \frac{\partial N_1}{\partial y} & \frac{\partial N_2}{\partial y} & \dots & \frac{\partial N_1}{\partial n} \\ \frac{\partial N_1}{\partial z} & \frac{\partial N_2}{\partial z} & \dots & \frac{\partial N_1}{\partial n} \end{bmatrix}}_{[B_{ij}^{e^\phi}]} \cdot \begin{pmatrix} \phi_1 \\ \phi_2 \\ \vdots \\ \phi_n \end{pmatrix} \tag{C.16}$$

The element residuals $\mathcal{R}_i^{e^\bullet}$ (where $\bullet$ is the degree of freedom considered) for the variational formulation are then

$$\mathcal{R}_i^{e^u} = -\int_{V^e} \left(\left[\underset{\sim}{\boldsymbol{B}}_s^{e^u}\right]^T \cdot \{\sigma^s\} + \left[\underset{\sim}{\boldsymbol{B}}_\omega^{e^u}\right]^T \cdot \{\pi_\theta\} \right) dV + \int_{\partial V} [N^{e^u}]^T \cdot \{t\}\, dS = 0 \tag{C.17}$$

$$\equiv \{{}^u F_i^e\} - \{{}^u F_e^e\} = 0 \tag{C.18}$$

$$\mathcal{R}_i^{e^\theta} = \int_{V^e} \left(\left[N^{e^\theta}\right]^T \cdot \{\pi_\theta\} - \left[\underset{\sim}{\boldsymbol{B}}^{e^\theta}\right]^T \cdot \{\xi_\theta\} \right) dV + \int_{\partial V} [N^{e^\theta}]^T \cdot \{M\} dS = 0 \tag{C.19}$$

$$\equiv \{{}^\theta F_i^e\} - \{{}^\theta F_e^e\} = 0 \tag{C.20}$$

$$\mathcal{R}_i^{e^\phi} = \int_{V^e} \left(-[B^{e^\phi}]^T \{\xi_\phi\} + \pi_\phi [N^{e^\phi}] \right) dV + \int_{\partial V^e} [N^{e^\phi}] \Xi_\phi dS = 0 \tag{C.21}$$

$$\equiv \{{}^\phi F_i^e\} - \{{}^\phi F_e^e\} = 0 \tag{C.22}$$

$$\tag{C.23}$$

where $\{^\bullet F_i^e\}$ and $\{^\bullet F_e^e\}$ are the vector of the internal reactions associated with the degrees of freedom $\bullet$ and the vector of the external forces in the element, respectively. The nonlinear system to be solved with Newton's method is then

$$\begin{Bmatrix} \mathcal{A}\left(\{^u F_i^e\}\right) \\ \mathcal{A}\left(\{^\theta F_i^e\}\right) \\ \mathcal{A}\left(\{^\phi F_i^e\}\right) \end{Bmatrix} - \begin{Bmatrix} \mathcal{A}\left(\{^u F_e^e\}\right) \\ \mathcal{A}\left(\{^\theta F_e^e\}\right) \\ \mathcal{A}\left(\{^\phi F_e^e\}\right) \end{Bmatrix} = 0 \tag{C.24}$$

where $\mathcal{A}$ denotes the assembly operator over all the elements. The Jacobian matrix $[K_t^e]$ of the element is obtained by derivation of the internal reactions with respect to the degrees of freedom:

$$[K_t^e] = \frac{\partial \left\{ \{^u F_i^e\} \quad \{^\theta F_i^e\} \quad \{^\phi F_i^e\} \right\}^T}{\partial \left\{ \{u\} \quad \{\theta\} \quad \{\phi\} \right\}^T} = \begin{bmatrix} [K_{uu}^e] & [K_{u\theta}^e] & [K_{u\phi}^e] \\ [K_{\theta u}^e] & [K_{\theta\theta}^e] & [K_{\theta\phi}^e] \\ [K_{\phi u}^e] & [K_{\phi\theta}^e] & [K_{\phi\phi}^e] \end{bmatrix} \tag{C.25}$$

with

$$[K_{uu}^e] = -\int_{V^e} \left[\underset{\sim}{\boldsymbol{B}}_s^{e^u}\right]^T \cdot \left[\frac{\partial \underset{\sim}{\boldsymbol{\sigma}}^s}{\partial \underline{\boldsymbol{u}} \otimes \nabla^s}\right] \cdot \left[\underset{\sim}{\boldsymbol{B}}_s^{e^u}\right] + \left[\underset{\sim}{\boldsymbol{B}}_\omega^{e^u}\right]^T \cdot \left[\frac{\partial \underline{\boldsymbol{\pi}}_\theta}{\partial \overset{\times}{\underline{\mathbf{e}}}}\right] \cdot \left[\underset{\sim}{\boldsymbol{B}}_\omega^{e^u}\right] dV \tag{C.26}$$

$$[K_{u\theta}^e] = \int_{V^e} -\left[\underset{\sim}{\boldsymbol{B}}_\omega^{e^u}\right]^T \cdot \left[-\frac{\partial \underline{\boldsymbol{\pi}}_\theta}{\partial \overset{\times}{\underline{\mathbf{e}}}}\right] \cdot \left[N^{e^\theta}\right] dV \tag{C.27}$$

$$[K_{u\phi}^e] = \int_{V^e} -\left[\underset{\sim}{\boldsymbol{B}}_\omega^{e^u}\right]^T \cdot \left(\left[\frac{\partial \underline{\boldsymbol{\pi}}_\theta}{\partial \phi}\right] \otimes \left[N^{e^\phi}\right]\right) dV \tag{C.28}$$

$$[K_{\theta u}^e] = \int_{V^e} \left[N^{e^\theta}\right]^T \cdot \left[\frac{\partial \underline{\boldsymbol{\pi}}_\theta}{\partial \overset{\times}{\underline{\mathbf{e}}}}\right] \cdot \left[\underset{\sim}{\boldsymbol{B}}_\omega^{e^u}\right] dV \tag{C.29}$$

$$[K_{\theta\theta}^e] = \int_{V^e} \left[N^{e^\theta}\right]^T \cdot \left[-\frac{\partial \underline{\boldsymbol{\pi}}_\theta}{\partial \overset{\times}{\underline{\mathbf{e}}}}\right] \cdot \left[N^{e^\theta}\right] - \left[\underset{\sim}{\boldsymbol{B}}^{e^\theta}\right]^T \cdot \left[\frac{\partial \underset{\sim}{\boldsymbol{\xi}}_\theta}{\partial \underline{\boldsymbol{\theta}} \otimes \nabla}\right] \left[\underset{\sim}{\boldsymbol{B}}^{e^\theta}\right] dV \tag{C.30}$$

$$[K_{\theta\phi}^e] = \int_{V^e} \left[N^{e^\theta}\right]^T \cdot \left(\left[\frac{\partial \underline{\boldsymbol{\pi}}_\theta}{\partial \phi}\right] \otimes \left[N^{e^\phi}\right]\right) - \left[\underset{\sim}{\boldsymbol{B}}^{e^\theta}\right]^T \cdot \left(\left[\frac{\partial \underset{\sim}{\boldsymbol{\xi}}_\theta}{\partial \phi}\right] \otimes \left[N^{e^\phi}\right]\right) dV \tag{C.31}$$

$$[K_{\phi u}^e] = \int_{V^e} [N^{e^\phi}] \otimes \left[\frac{\partial \pi_\phi}{\partial \overset{\times}{\underline{\omega}}}\right] \cdot \left[\underset{\sim}{\boldsymbol{B}}_\omega^{e^u}\right] dV \tag{C.32}$$

$$[K_{\phi\theta}^e] = \int_{V^e} [N^{e^\phi}] \otimes \left[\frac{\partial \pi_\phi}{\partial \underline{\boldsymbol{\theta}}}\right] \cdot [N^{e^\theta}] + [N^{e^\phi}] \otimes \left[\frac{\partial \pi_\phi}{\partial \underline{\boldsymbol{\theta}} \otimes \nabla}\right] \cdot \left[\underset{\sim}{\boldsymbol{B}}^{e^\theta}\right] dV \tag{C.33}$$

$$[K_{\phi\phi}^e] = \int_{V^e} -[B^{e^\phi}]^T \cdot \left[\frac{\partial \underline{\boldsymbol{\xi}}_\phi}{\partial \nabla \phi}\right] \cdot [B^{e^\phi}] + \frac{\partial \pi_\phi}{\partial \phi} \left([N^{e^\phi}] \otimes [N^{e^\phi}]\right) dV \tag{C.34}$$

References

Abrivard, G., Busso, E.P., Forest, S., Appolaire, B., 2012a. Phase field modelling of grain boundary motion driven by curvature and stored energy gradients. part i: theory and numerical implementation. Philosophical Magazine 92, 3618–3642.

Abrivard, G., Busso, E.P., Forest, S., Appolaire, B., 2012b. Phase field modelling of grain boundary motion driven by curvature and stored energy gradients. part ii: Application to recrystallisation. Philosophical Magazine 92, 3643–3664.

Admal, N.C., Po, G., Marian, J., 2018. A unified framework for polycrystal plasticity with grain boundary evolution. International Journal of Plasticity 106, 1–30.

Admal, N.C., Segurado, J., Marian, J., 2019. A three-dimensional misorientation axis- and inclination-dependent Kobayashi-Warren-Carter grain boundary model. Journal of the Mechanics and Physics of Solids 128, 32 – 53. doi:10.1016/j.jmps.2019.03.020.

Anderson, M.P., Srolovitz, D.J., Grest, G.S., Sahni, P.S., 1984. Computer simulation of grain growth–i. kinetics. Acta Metallurgica 32, 783–791.

Ashby, M., 1970. The deformation of plastically non–homogeneous materials. Philosophical Magazine 21, 399–424. doi:10.1080/14786437008238426.

Ask, A., Forest, S., Appolaire, B., Ammar, K., 2018a. Cosserat crystal plasticity with dislocation–driven grain boundary migration. Journal of Micromechanics and Molecular Physics 3, 1840009. doi:10.1142/S242491301840009X.

Ask, A., Forest, S., Appolaire, B., Ammar, K., 2019. A Cosserat–phase field theory of crystal plasticity and grain boundary migration at finite deformation. Continuum Mechanics and Thermodynamics 31, 1109–1141. doi:10.1007/s00161-018-0727-6.

Ask, A., Forest, S., Appolaire, B., Ammar, K., 2020. Microstructure evolution in deformed polycrystals predicted by a diffuse interface Cosserat approach. Advanced Modeling and Simulation in Engineering Sciences 7, 1–28.

Ask, A., Forest, S., Appolaire, B., Ammar, K., Salman, O.U., 2018b. A Cosserat crystal plasticity and phase field theory for grain boundary migration. Journal of the Mechanics and Physics of Solids 115, 167–194. doi:doi.org/10.1016/j.jmps.2018.03.006.

Baek, J., Chen, J.S., Tupek, M., Beckwith, F., Fang, H.E., 2022. A duality-based coupling of Cosserat crystal plasticity and phase field theories for modeling grain refinement. International Journal for Numerical Methods in Engineering 123, 953–991. doi:10.1002/nme.6884.

Beck, P.A., 1949. The formation of recrystallization nuclei. Journal of Applied Physics 20, 633–634.

Beck, P.A., Sperry, P.R., 1950. Strain induced grain boundary migration in high purity aluminum. Journal of Applied Physics 21, 150–152.

Bernacki, M., Chastel, Y., Coupez, T., Logé, R.E., 2008. Level set framework for the numerical modelling of primary recrystallization in polycrystalline materials. Scripta Materialia 58, 1129–1132.

Besson, J., Cailletaud, G., Chaboche, J.L., Forest, S., Blétry, M., 2009. Non–Linear Mechanics of Materials. Solid Mechanics and Its Applications 167, Springer-Verlag Berlin Heidelberg. doi:10.1007/978-90-481-3356-7.

Besson, J., Foerch, R., 1997. Large scale object-oriented finite element code design. Computer Methods in Applied Mechanics and Engineering 142, 165–187.

Blesgen, T., 2015. On rotation deformation zones for finite-strain Cosserat plasticity. Acta Mechanica 226, 2421–2434.

Blesgen, T., 2017. A variational model for dynamic recrystallization based on Cosserat plasticity. Composites Part B: Engineering 115, 236–243.

Bonarski, B., Schafler, E., Mikulowski, B., Zehetbauer, M., 2008. Texture evolution of magnesium single crystals deformed by high-pressure torsion. Materials Science Forum 584-586, 263–268. doi:10.4028/www.scientific.net/msf.584-586.263.

Cahn, R.W., 1950. A new theory of recrystallization nuclei. Proceedings of the Physical Society. Section A 63, 323.

Chen, L., Chen, J., Lebensohn, R.A., Ji, Y.Z., Heo, T.W., Bhattacharyya, S., Chang, K., Mathaudhu, S., Liu, Z.K., Chen, L.Q., 2015. An integrated fast fourier transform-based phase-field and crystal plasticity approach to model recrystallization of three dimensional polycrystals. Computer Methods in Applied Mechanics and Engineering 285, 829–848.

Chen, L.Q., Yang, W., 1994. Computer simulation of the domain dynamics of a quenched system with a large number of nonconserved order parameters: The grain-growth kinetics. Physical Review B 50, 15752.

Cheong, K.S., Busso, E.P., 2004. Discrete dislocation density modelling of single phase FCC polycrystal aggregates. Acta Materialia 52, 5665–5675.

Doherty, R.D., Hughes, D.A., Humphreys, F.J., Jonas, J.J., Jensen, D.J., Kassner, M.E., King, W.E., McNelley, T.R., McQueen, H.J., Rollett, A.D., 1997. Current issues in recrystallization: a review. Materials Science and Engineering: A 238, 219–274.

Elder, K., Grant, M., Provatas, N., Kosterlitz, J., 2001. Sharp interface limits of phase-field models. Physical Review E 64, 021604.

Ferdinand Knipschildt, E.F., 2022. Nucleation of recrystallization. Materials Science and Technology 38, 765–779.

Forest, S., 1998. Modeling slip, kink and shear banding in classical and generalized single crystal plasticity. Acta Materialia 46, 3265–3281.

Forest, S., Barbe, F., Cailletaud, G., 2000. Cosserat modelling of size effects in the mechanical behaviour of polycrystals and multiphase materials. International Journal of Solids and Structures 37, 7105–7126.

Forest, S., Cailletaud, G., Sievert, R., 1997. A Cosserat theory for elastoviscoplastic single crystals at finite deformation. Archives of Mechanics 49, 705–736.

Forest, S., Ghiglione, F., 2023. Size effects in cosserat crystal plasticity, in: Sixty Shades of Generalized Continua: Dedicated to the 60th Birthday of Prof. Victor A. Eremeyev. Springer, pp. 211–234.

Fressengeas, C., Taupin, V., Capolungo, L., 2011. An elasto-plastic theory of dislocation and disclination fields. International Journal of Solids and Structures 48, 3499–3509.

Gao, J., Thompson, R., 1996. Real time-temperature models for monte carlo simulations of normal grain growth. Acta Materialia 44, 4565–4570.

Gérard, C., Bacroix, B., Bornert, M., Cailletaud, G., Crépin, J., Leclercq, S., 2009. Hardening description for FCC materials under complex loading paths. Computational Materials Science 45, 751 – 755. doi:10.1016/j.commatsci.2008.08.027.

Ghiglione, F., Forest, S., 2022. On the torsion of isotropic elastoplastic Cosserat circular cylinders. Journal of Micromechanics and Molecular Physics 6, 1–14. doi:10.1142/S2424913021420078.

Giga, Y., Okamoto, J., Uesaka, M., 2023. A finer singular limit of a single-well modica–mortola functional and its applications to the kobayashi–warren–carter energy. Advances in Calculus of Variations 16, 163–182.

Gottstein, G., Shvindlerman, L.S., 2009. Grain boundary migration in metals: thermodynamics, kinetics, applications. CRC press.

Gourdet, S., Montheillet, F., 2000. An experimental study of the recrystallization mechanism during hot deformation of aluminium. Materials Science and Engineering: A 283, 274–288. doi:doi.org/10.1016/S0921-5093(00)00733-4.

Günther, W., 1958. Zur statik und kinematik des cosseratschen kontinuums. Abhandlungen der Braunscheigschen Wissenschaftlichen Gesellschaft 10, 1.

Gurtin, M.E., 1996. Generalized Ginzburg–Landau and Cahn–Hilliard equations based on a microforce balance. Physica D 92, 178–192.

He, J., Admal, N.C., 2021a. Polycrystal plasticity and grain boundary evolution: A unified dislocation-based diffuse-interface approach. arXiv preprint arXiv:2102.00666 .

He, J., Admal, N.C., 2021b. Polycrystal plasticity with grain boundary evolution: a numerically efficient dislocation-based diffuse-interface model. Modelling and Simulation in Materials Science and Engineering 30, 025006.

Hesselbarth, H.W., Göbel, I., 1991. Simulation of recrystallization by cellular automata. Acta Metallurgica et Materialia 39, 2135–2143.

Kafadar, C.B., Eringen, A.C., 1971. Micropolar media: I the classical theory. International Journal of Engineering Science 9, 271–305.

Kassner, M.E., 1989. Large-strain deformation of aluminum single crystals at elevated temperature as a test of the geometric-dynamic-recrystallization concept. Metallurgical Transactions A 20, 2182–2185. doi:10.1007/BF02650307.

Kassner, M.E., Barrabes, S.R., 2005. New developments in geometric dynamic recrystallization. Materials Science and Engineering: A 410-411, 152–155. doi:10.1016/j.msea.2005.08.052.

Kim, J., Jacobs, M., Osher, S., Admal, N.C., 2021. A crystal symmetry-invariant kobayashi-warren-carter grain boundary model and its implementation using a thresholding algorithm. Computational Materials Science 199, 110575.

Kobayashi, R., Warren, J.A., Carter, W.C., 2000. A continuum model of grain boundaries. Physica D: Nonlinear Phenomena 140, 141–150.

Kröner, E., 1963. On the physical reality of torque stresses in continuum mechanics. International Journal of Engineering Science 1, 261–278.

Li, Y., Hu, S., Barker, E., Overman, N., Whalen, S., Mathaudhu, S., 2020. Effect of grain structure and strain rate on dynamic recrystallization and deformation behavior: A phase field-crystal plasticity model. Computational Materials Science 180, 109707.

Liu, P., Lusk, M.T., 2002. Parametric links among monte carlo, phase-field, and sharp-interface models of interfacial motion. Physical Review E 66, 061603.

Liu, Y., Baudin, T., Penelle, R., 1996. Simulation of normal grain growth by cellular automata. Scripta Materialia 34, 1679–1683.

Lobkovsky, A.E., Warren, J.A., 2001. Sharp interface limit of a phase-field model of crystal grains. Physical Review E 63, 051605.

Luan, Q., Lee, J., Zheng, J.H., Hopper, C., Jiang, J., 2020. Combining microstructural characterization with crystal plasticity and phase-field modelling for the study of static recrystallization in pure aluminium. Computational Materials Science 173, 109419.

Mason, J., Lind, J., Li, S., Reed, B., Kumar, M., 2015. Kinetics and anisotropy of the monte carlo model of grain growth. Acta Materialia 82, 155–166.

Mayeur, J.R., McDowell, D.L., 2014. A comparison of gurtin type and micropolar theories of generalized single crystal plasticity. International Journal of Plasticity 57, 29–51. doi:10.1016/j.ijplas.2014.01.010.

Mayeur, J.R., McDowell, D.L., Bammann, D.J., 2011. Dislocation–based micropolar single crystal plasticity: Comparison of multi– and single criterion theories. Journal of the Mechanics and Physics of Solids 59, 398–422.

Montheillet, F., Cohen, M., Jonas, J., 1984. Axial stresses and texture development during the torsion testing of Al, Cu and α-Fe. Acta Metallurgica 32, 2077–2089. doi:10.1016/0001-6160(84)90187-1.

Ngenzi, E., El Omari, Z., Bacroix, B., Queyreau, S., 2021. Mobility functions for [001] CSL grain boundaries in Ni from molecular dynamics. URL: `https://hal.science/hal-03505810`. working paper or preprint.

Ngenzi, E., Queyreau, S., 2023. Comparison of Atomistic and Phase Field Descriptions of [001] Symmetric Tilt Grain Boundary in Ni. URL: `https://hal.science/hal-03917090`. working paper or preprint.

Nouailhas, D., Cailletaud, G., 1995. Tension-torsion behavior of single-crystal superalloys - Experiment and finite-element analysis. International Journal of Plasticity 8, 451–470.

Nye, J., 1953. Some geometrical relations in dislocated crystals. Acta Metallurgica 1, 153–162.

Petryk, H., Stupkiewicz, S., 2016. A minimal gradient-enhancement of the classical continuum theory of crystal plasticity. Part I: The hardening law. Archives of Mechanics 68, 459–585.

Phalke, V., Kaiser, T., Scherer, J.M., Forest, S., 2021. Modeling size effects in microwire torsion: A comparison between a lagrange multiplier-based and a Curl$\mathbf{F}^{\mathrm{p}}$ gradient crystal plasticity model. European Journal of Mechanics A/Solids 94, 104550. doi:10.1016/j.euromechsol.2022.104550.

Raabe, D., 1998. Discrete mesoscale simulation of recrystallization microstructure and texture using a stochastic cellular automation approach, in: Materials Science Forum, Trans Tech Publ. pp. 169–174.

Raabe, D., 2000. Scaling Monte Carlo kinetics of the Potts model using rate theory. Acta Materialia 48, 1617–1628.

Raabe, D., 2014. 23 - Recovery and recrystallization: Phenomena, physics, models, simulation, in: Laughlin, D.E., Hono, K. (Eds.), Physical Metallurgy (Fifth Edition). Elsevier, Oxford, pp. 2291–2397. doi:10.1016/B978-0-444-53770-6.00023-X.

Rios, P.R., Siciliano Jr, F., Sandim, H.R.Z., Plaut, R.L., Padilha, A.F., 2005. Nucleation and growth during recrystallization. Materials Research 8, 225–238.

Rollett, A., Rohrer, G.S., Humphreys, J., 2017. Recrystallization and Related Annealing Phenomena. Elsevier.

Rys, M., Stupkiewicz, S., Petryk, H., 2022. Micropolar regularization of crystal plasticity with the gradient-enhanced incremental hardening law. International Journal of Plasticity 156, 103355. doi:10.1016/j.ijplas.2022.103355.

Sarrazola, D.A.R., Maire, L., Moussa, C., Bozzolo, N., Muñoz, D.P., Bernacki, M., 2020a. Full field modeling of dynamic recrystallization in a CPFEM context–application to 304l steel. Computational Materials Science 184, 109892.

Sarrazola, D.R., Muñoz, D.P., Bernacki, M., 2020b. A new numerical framework for the full field modeling of dynamic recrystallization in a CPFEM context. Computational Materials Science 179, 109645.

Scherer, J.M., Phalke, V., Besson, J., Forest, S., Hure, J., Tanguy, B., 2020. Lagrange multiplier based vs micromorphic gradient-enhanced rate-(in)dependent crystal plasticity modelling and simulation. Computer Methods in Applied Mechanics and Engineering 372, 113426. doi:10.1016/j.cma.2020.113426.

Scholtes, B., Boulais-Sinou, R., Settefrati, A., Muñoz, D.P., Poitrault, I., Montouchet, A., Bozzolo, N., Bernacki, M., 2016. 3d level set modeling of static recrystallization considering stored energy fields. Computational Materials Science 122, 57–71.

Sitko, M., Chao, Q., Wang, J., Perzynski, K., Muszka, K., Madej, L., 2020. A parallel version of the cellular automata static recrystallization model dedicated for high performance computing platforms–development and verification. Computational Materials Science 172, 109283.

Steinbach, I., Apel, M., 2006. Multi phase field model for solid state transformation with elastic strain. Physica D 217, 153–160.

Steinbach, I., Pezzolla, F., 1999. A generalized field method for multiphase transformations using interface fields. Physica D: Nonlinear Phenomena 134, 385–393.

Stupkiewicz, S., Petryk, H., 2016. A minimal gradient-enhancement of the classical continuum theory of crystal plasticity. Part II: Size effects. Archives of Mechanics 68, 487–513.

Takaki, T., Hirouchi, T., Hisakuni, Y., Yamanaka, A., Tomita, Y., 2008a. Multi-phase-field model to simulate microstructure evolutions during dynamic recrystallization. Materials Transactions 49, 2559–2565.

Takaki, T., Tomita, Y., 2010. Static recrystallization simulations starting from predicted deformation microstructure by coupling multi-phase-field method and finite element method based on crystal plasticity. International Journal of Mechanical Sciences 52, 320–328.

Takaki, T., Yamanaka, A., Higa, Y., Tomita, Y., 2008b. Phase-field model during static recrystallization based on crystal-plasticity theory. Journal of Computer–Aided Materials Design 14, 75–84.

Taupin, V., Capolungo, L., Fressengeas, C., Das, A., Upadhyay, M., 2013. Grain boundary modeling using an elasto-plastic theory of dislocation and disclination. Journal of the Mechanics and Physics of Solids 61, 370–384.

Vandermeer, R., Jensen, D.J., Woldt, E., 1997. Grain boundary mobility during recrystallization of copper. Metallurgical and Materials Transactions A 28, 749–754.

Warren, J.A., Kobayashi, R., Lobkovsky, A.E., Carter, W.C., 2003. Extending phase field models of solidification to polycrystalline materials. Acta Materialia 51, 6035–6058.

Wolf, D., 1990. Structure-energy correlation for grain boundaries in fcc metals–iii. symmetrical tilt boundaries. Acta Metallurgica et Materialia 38, 781–790.

Z-set, 2022. Non-linear material & structure analysis suite. URL: `www.zset-software.com`.